

Original Article

Transient oscillation dynamics during sleep provide a robust basis for electroencephalographic phenotyping and biomarker identification

Patrick A. Stokes¹, Preetish Rath^{1,2}, Thomas Possidente¹, Mingjian He^{1,3,4}, Shaun Purcell⁵, Dara S. Manoach⁶, Robert Stickgold⁷ and Michael J. Prerau^{1,*}

¹Division of Sleep and Circadian Disorders, Brigham and Women's Hospital, Boston, MA, USA,

²Department of Computer Science, Tufts University, Medford, MA, USA,

³Harvard-MIT Health Sciences and Technology, Massachusetts Institute of Technology, Cambridge, MA, USA,

⁴Department of Anesthesia, Critical Care and Pain Medicine, Massachusetts General Hospital, Boston, MA, USA,

⁵Department of Psychiatry, Brigham and Women's Hospital, Boston, MA, USA,

⁶Department of Psychiatry, Massachusetts General Hospital, Boston, MA, USA and

⁷Department of Psychiatry, Beth Israel Deaconess Medical Center, Boston, MA, USA

*Corresponding author: Michael J. Prerau, Brigham and Women's Hospital, Division of Sleep and Circadian Disorders, 221 Longwood Avenue, Boston, MA, 02115, USA. Email: mprerau@bwh.harvard.edu.

Abstract

Transient oscillatory events in the sleep electroencephalogram represent short-term coordinated network activity. Of particular importance, sleep spindles are transient oscillatory events associated with memory consolidation, which are altered in aging and in several psychiatric and neurodegenerative disorders. Spindle identification, however, currently contains implicit assumptions derived from what waveforms were historically easiest to discern by eye, and has recently been shown to select only a high-amplitude subset of transient events. Moreover, spindle activity is typically averaged across a sleep stage, collapsing continuous dynamics into discrete states. What information can be gained by expanding our view of transient oscillatory events and their dynamics? In this paper, we develop a novel approach to electroencephalographic phenotyping, characterizing a generalized class of transient time-frequency events across a wide frequency range using continuous dynamics. We demonstrate that the complex temporal evolution of transient events during sleep is highly stereotyped when viewed as a function of slow oscillation power (an objective, continuous metric of depth-of-sleep) and phase (a correlate of cortical up/down states). This two-fold power-phase representation has large intersubject variability—even within healthy controls—yet strong night-to-night stability for individuals, suggesting a robust basis for phenotyping. As a clinical application, we then analyze patients with schizophrenia, confirming established spindle (12–15 Hz) deficits as well as identifying novel differences in transient non-rapid eye movement events in low-alpha (7–10 Hz) and theta (4–6 Hz) ranges. Overall, these results offer an expanded view of transient activity, describing a broad class of events with properties varying continuously across spatial, temporal, and phase-coupling dimensions.

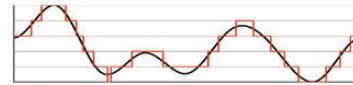
Key words: spindles; transient oscillations; TF-peaks; EEG; NREM; slow oscillation; phase coupling

Graphical Abstract

Our understanding of spindle-like activity is based on limiting historical assumptions from visual EEG inspection and discrete staging.

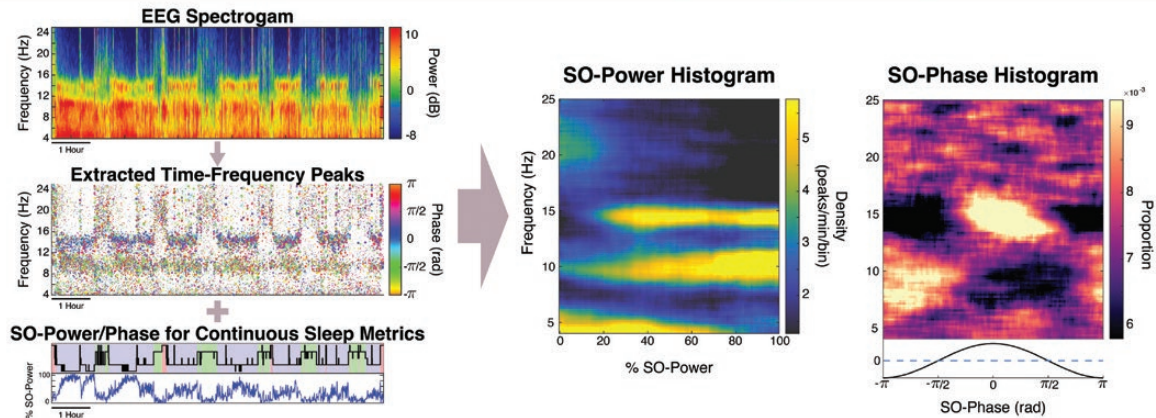


Spindles are defined based on visual observations of waveforms from the 1930s

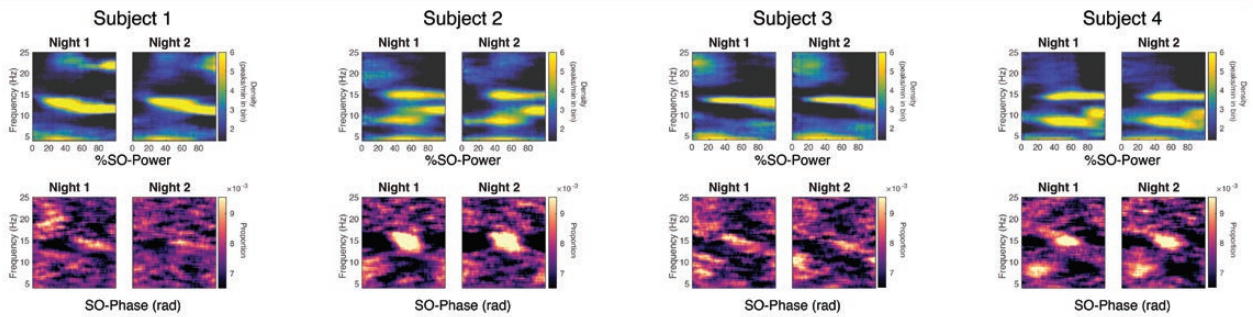


Staging discretizes continuous sleep processes

We develop a novel approach to EEG phenotyping, called Slow Oscillation Power & Phase Histograms, which map the activity of tens of thousands of transient oscillations to continuous metrics of depth-of-sleep and cortical up/down states.



By doing so, we find a trait-like representation with vast heterogeneity between participants, yet strong night-to-night consistency.



These results reveal a broad class of events with properties varying continuously across spatial, temporal, and phase-coupling dimensions, thus making this approach a promising new tool for neuroscience, patient phenotyping, and biomarker identification.

Statement of Significance

Sleep spindles are a vital component in memory consolidation, and deviations in spindle dynamics have been linked to aging, as well as neurodevelopmental, psychiatric, and neurodegenerative disorders. In this paper, we demonstrate a transformative, novel characterization of a broad range of spindle-like activity, creating a compact and comprehensive representation of the continuous dynamics of tens of thousands of transient sleep oscillation events across the night. Instead of using discrete sleep stages, we use continuous metrics of depth-of-sleep and network activity. We show that this characterization is highly heterogeneous between subjects, yet trait-like night-to-night for a given individual. This approach is therefore a promising new tool for neuroscience, patient phenotyping, and biomarker identification.

Introduction

The identification of oscillatory activity within the electroencephalogram (EEG) has long been a means of characterizing the dynamics of neural activity across multiple time scales [1, 2]. Traditionally, EEG oscillatory activity is classified according to a set of canonical frequency ranges [3, 4], typically: slow oscillation (SO) (<1.5 Hz) [5], delta (<4 Hz), theta (4–8 Hz), alpha (8–12 Hz), sigma (11–16 Hz), beta

(15–30 Hz), and gamma (>30 Hz). In addition to these persistent oscillatory components, the EEG also contains short bursts of oscillatory activity, which we term *transient oscillations*. Due to their short duration, transient oscillations tend to have a low signal-to-noise ratio and have thus been difficult to conclusively observe or define.

Transient oscillations have been shown to have great physiological importance. Perhaps the most noteworthy transient oscillations are sleep spindles—waxing-waning waveforms of sigma

activity that define non-rapid eye movement (NREM) stage 2 (N2) sleep [6–8]. Spindle activity has been linked to memory consolidation during sleep [7, 9] and deficits are associated with numerous disorders, such as schizophrenia (SZ) [10–16], Alzheimer’s disease [17–19], and autism [20, 21], as well as with natural aging [5, 22–26]. Given their functional and clinical significance, it is critical to understand how, when, and where spindles appear during the night. In doing so, it may be possible to identify useful electrophysiological phenotypes of transient oscillation activity and dynamics [22, 27–29], variations of which may serve as biomarkers of disease or indicators of health.

There are several challenges that have limited the scope and power of transient oscillation analyses. Spindles, like many sleep EEG features, were first identified in the early 1900s through visual observation of waveform traces on paper [30, 31]. Almost a century later, the gold standard for spindle identification remains subjective waveform identification by experts [6, 32], which is also the standard by which automated methods are typically evaluated [33]. Transient oscillations, however, are easily obfuscated in the time-domain by activity at other frequencies, creating definitions that have been shown to impose an implicit selection bias toward high-amplitude, visually salient waveforms [34]. We must therefore ask the question: what transient oscillatory activity exists beyond those waveforms easily observed by the eye? Furthermore, while the thalamocortical origins of spindles are well-established [7, 35–38], spindle analysis from EEG alone currently proceeds largely without the ability to justify the inclusion or exclusion of a particular waveform event, as the underlying neurophysiological generators are unobserved. How then, can we improve our understanding of spindle-like events in the absence of a ground truth?

To address these questions, we look toward more general analyses of a broader class of transient events. We leverage the fact that transient oscillations will appear, by definition, as three-dimensional peaks in the time-frequency (TF) domain topography [39]. We refer to the general class of these salient, localized peaks as *TF-peaks* [32], which appear as “blobs” in a two-dimensional (2D) spectrogram (Figure 1A–C) [34, 40]. Recent work has demonstrated a direct link between TF-peaks and spindle activity, showing that TF-peaks in the sigma range (TF σ peaks) provide more robust characterization of spindle-like activity than traditionally detected spindles [34]. This approach also expands on previous work from Olbrich and Achermann, which used autoregressive modeling to identify and characterize sleep EEG oscillatory events and their properties [41–43]. We, therefore, use TF-peaks as the foundation of our analyses, which we identify using a novel variant on the watershed algorithm [44–46] that allows a more flexible TF-peak structure than previous parametric-based approaches [43, 47]. We can then build distributions on the properties of TF-peaks at all frequencies (Figure 1D), the structure of which can be compared across different conditions or brain states. In analyzing all TF-peaks together as a distribution, we can mitigate some of the issues inherent in the detection of individual events in the absence of ground truth.

To improve the context of TF-peaks within a given brain state, we can attempt to increase the resolution of depth-of-sleep beyond traditional sleep staging by using a continuum representation of sleep microarchitecture. Current clinical standards categorize brain state into wake (W), rapid eye movement (REM), and NREM stages 1–3 (N1–N3) in fixed 30 s epochs, based on visual inspection by experts using agreed-upon criteria [6, 32]. Analyses of brain activity typically average within stage, which collapses continuously evolving sleep into low-dimensional discrete states.

We can instead replace discrete stages with an objective continuous metric of brain state, thereby enhancing our ability to observe gradual changes during sleep. While numerous candidate metrics have been proposed for estimating continuous depth-of-consciousness and sleep (e.g. bispectral index, spectral edge/median/slope, state-space modeling, entropy, and statistical measures.) [48–59], we use SO-power due to its simplicity, objectivity, and long-standing use as a surrogate of slow-wave-sleep depth and the hypnogenic Process S [60–63]. SO-power is particularly useful in this application as it provides an enhanced, continuous characterization of NREM sleep, the key focus of transient oscillation analyses. Similarly, we can use the SO-phase to characterize short timescale dynamics, given its established relationship to cross-frequency coupling in spindles with respect to cortical up/down states, changes in which have been related to aging as well as pathological states [5, 12, 64–67]. By relating TF-peak activity to these continuous objective metrics (SO phase and power), we can more precisely characterize transient oscillation dynamics across different time scales and brain states.

Herein, we combine the concepts of TF-peaks, distributional analysis, and metrics of continuous sleep dynamics to develop a novel approach to EEG phenotyping. Our approach is as follows: (1) Identify TF-peaks in the sleep EEG spectrogram across time and frequency, (2) Extract SO-power and SO-phase to represent objective continuous metrics of long and short-scale neural dynamics, and (3) Characterize the distribution of TF-peak rate (density) as a function of TF-peak oscillation frequency and SO-power or SO-phase. In doing so, we can create a comprehensive representation of transient oscillation dynamics at different time scales, providing a highly informative new technique and powerful basis for EEG phenotyping and biomarker identification in pathological states.

Methods

Experimental data

We acquired data for 17 healthy control (HC) participants and 21 medicated participants with schizophrenia (SZ) from a previously published study by Wamsley et al [11]. Data from 1 HC and 1 SZ participant were excluded based on our data quality criterion requiring fewer than 3 h of scored wake after sleep onset. Thus, we analyzed data from 16 HC participants (age: 36 ± 7 , 3F/14M) and 20 SZ patients (age: 33 ± 9 , 4F/16M). Healthy participants screened to exclude a personal history of mental illness, a family history of SZ spectrum disorder, and psychoactive medication use, were recruited from the community. Patients had been maintained on stable doses of atypical antipsychotic medications for at least 6 weeks and 12 took diverse adjunctive medications for anxiety, agitation, and/or concurrent mood disturbance. All participants underwent polysomnography for two consecutive nights. EEG data were digitally acquired at a sampling rate of 100 Hz using an Embla N7000 system (Medcare Systems, Buffalo, NY) with a standard montage including five to seven channels of EEG (F3/4 [11 HC, 14 SZ], C3/4 [16 HC, 20 SZ], Pz [14 HC, 14 SZ], O1/2 [16 HC, 16 SZ]) referenced to the linked mastoids. Data from all available electrodes were analyzed for each participant.

Artifact rejection was performed automatically, using an iterative procedure on the time-series data. First, the data are high pass filtered into two components: a high frequency (25 Hz to Nyquist) component and a broadband (0.1 Hz to Nyquist) component. For each component, any data exceeding a threshold—3.5 standard deviations above/below the mean—is marked as an artifact and removed. This procedure is performed iteratively on the

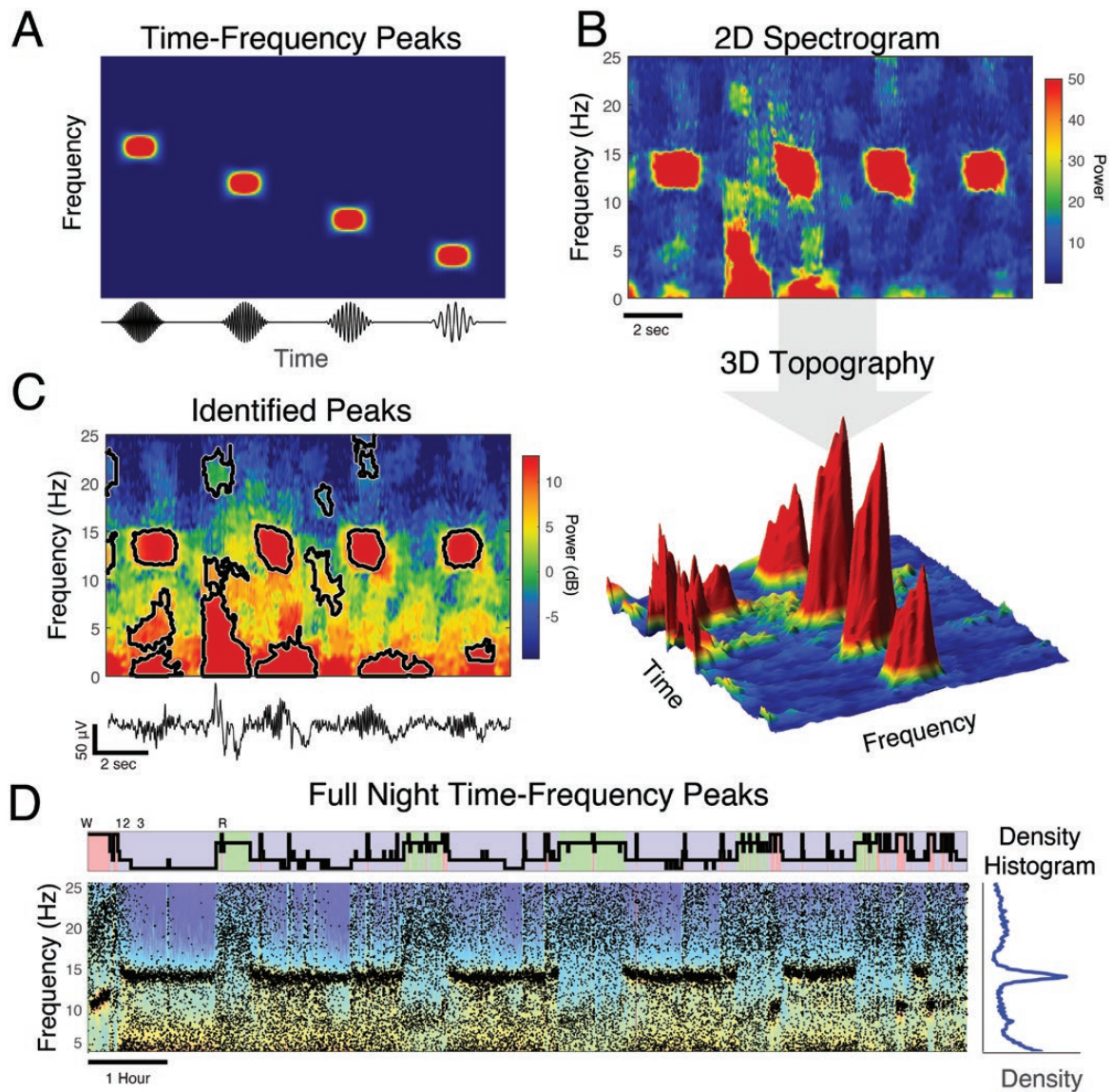


Figure 1. Identifying transient oscillatory activity using topographic peaks in the time-frequency histogram. (A) Simulated data show that transient oscillatory waveforms will definitionally appear as well-defined peaks in the spectrogram. (B) After baseline removal, time-frequency peaks (TF-peaks) in the spectral topography (top: 2D spectrogram and bottom: 3D surface) can be identified in experimental sleep EEG data using a watershed approach. The weighted centroid of each peak is used to determine the central frequency and time of each peak. (C) The volume-localized borders are displayed (black curves) over the original spectrogram, which corresponds to TF-peaks in the time-domain trace. (D) A scatter plot of ~60 k peak centroids (x = time; y = frequency; size = peak magnitude) from the full-night mapped to the full spectrogram and used to compute a density histogram (right panel), which shows the aggregate distributional structure of the TF-peaks over the whole night.

remaining time points, recomputing the threshold at each time, until no data exceeds the threshold. Any time points marked as an artifact for either component are designated as an artifact.

TF-peak identification

For all participants, electrodes, and nights, TF-peaks were identified using a novel approach based on the watershed transformation, a long-standing method used in image processing applications [44–46]. In brief, the approach treats the spectrogram topography like a geographic terrain and estimates the “catchment basins” into which rainwater would collect as it flows downward. In doing so, we can identify topographically distinct peaks, from which features may be extracted. For each TF-peak, we compute the oscillation frequency, as well as the corresponding SO-power and phase. Peaks with properties not resolvable within

the parameters of the spectral estimator were removed as noise, as well as peaks occurring during wake and artifact periods. Analysis focused on peaks between 4 and 25 Hz, with the low end cutoff imposed to mitigate spectral bleeding from the SO. Details of the approach can be found in [Appendix 1](#).

Analysis of TF-peak dynamics: SO-power and phase histograms

The *SO-power histogram* is a construct that allows us to observe patterns in TF-peak occurrence by looking at the rate as a function of TF-peak central frequency and (0.3–1.5 Hz) SO-power. To form this 2D histogram, we first create a matrix of discrete bins in frequency (rows) and bins in SO-power (columns). For all TF-peaks, we then extract the central frequency and SO-power at the time at which the peak occurred. We then create a two-dimensional

histogram by counting the number of TF-peaks that fall into each frequency \times SO-power bin. We convert the counts to a rate by normalizing each column by the amount of time spent within the corresponding SO-power for each bin. Figure 2A and B show a schematic of the basis for this histogram using simulated data.

The SO-phase histogram (Figure 2D) is a two-dimensional histogram analogous to the SO-power histogram but using TF-peak centroid frequency versus the SO-phase at the time of occurrence. Since the phase is circular, we compute bins that wrap around

$+\pi$. In this case, we convert the TF-peak density to proportion by normalizing it so that each row integrates into one. Figure 2C and D show a schematic of forming these histograms using simple simulated data.

Details of SO-power and SO-phase histogram construction can be found in Appendix 2. We present the color scales using perceptually uniform color maps, designed to increase accuracy of presentation and visual accessibility [68].

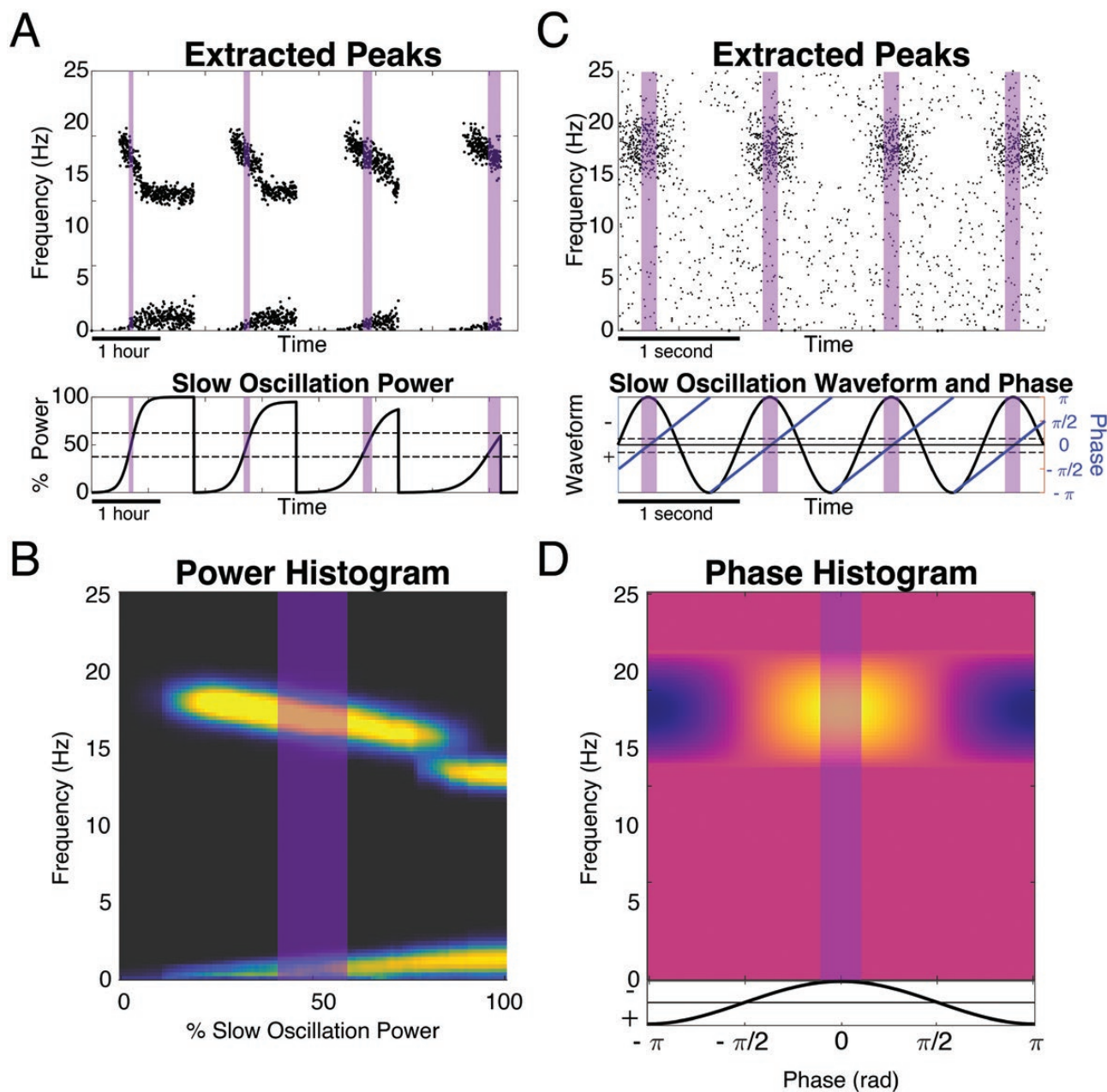


Figure 2. The construction of slow oscillation (SO) power and phase histograms. To characterize TF-peak density as a function of depth of sleep and frequency, we can construct a SO-power histogram. (A) Given a set of TF-peaks (upper panel) and %SO-power trace (lower panel) over time, we can construct a two-dimensional histogram by defining a set of frequency \times %SO-power bins. We first find all the times in which %SO-power falls within a given bin. For example, shaded regions in (A) and (B) represent a %SO-power bin of 40%–60%. Each column of the SO-power histogram is then computed by taking the TF-peak count in each frequency bin divided by the total time the %SO-power fell within that bin. Similarly, we can characterize TF-peak phase coupling using a SO-phase histogram. (C) Given a set of TF-peaks (upper panel) and their corresponding SO-phase (lower panel and blue curve), we can compute a two-dimensional histogram using frequency \times SO-phase bins. (D) We compute the SO-phase histogram by computing the density in the corresponding bins. As an example, shaded regions in (C) and (D) represent a SO-phase bin of $-\pi/8$ to $\pi/8$. The densities are then normalized row-wise to get the proportion of activity within a given bin.

Statistical analyses

SO-power and phase comparisons

To make group comparisons of the SO-phase and SO-power histograms between electrodes, we compute statistical significance by controlling for a 10% false discovery rate on the bins of the histograms. We use the procedure described in Benjamini and Yekutieli [69], which does not assume independence between samples. This is appropriate as dependence structure is expected between frequency and SO-power/phase in the histogram, and more generally between neighboring bins with overlapping bounds.

Feature distribution comparisons

Comparison of aggregate TF-peak single-feature distributions, such as the density histograms, are performed using the Kolmogorov Smirnov (KS) test [70], which is performed on the counts per histogram bin. Given a large number of peaks in each distribution (60,000+ per record) and the discrete values of some features, the KS test applied to the raw peak features is overly sensitive to small deviations. Thus, the use of the histograms is more conservative, reflecting some of the uncertainty of the underlying distributions, while still having relatively high degrees of freedom.

Clinical population density analysis

For the comparison of HC and SZ cohorts, regions in the SO-power/frequency space were defined to identify the activity of the major observed modes in the SO-power histogram. The modes were defined using the following frequency and power ranges— σ_{fast} : 15%–100%, 12–15 Hz, σ_{slow} : 60%–100%, 10–12 Hz, α_{low} : 20%–85%, 7–10 Hz, θ : 0%–80%, 4–6 Hz. TF-peak density was computed for each mode by summing up the total TF-peak count in the region and dividing it by the total time across all SO-power bins within that region. Density was computed in this way for each subject for all mode regions. HC and SZ densities were compared via t-test. No statistical differences in sleep architecture were observed between HC and SZ populations for this data set [11].

Code availability

We have developed an open source Transient Oscillation Dynamics (TOD) toolbox for identifying TF-peaks and for creating SO-power/phase histograms. The toolbox and a set of tutorials are available at <http://sleepEEG.org>

Data availability

De-identified and coded EEG data are available upon reasonable request by contacting Dr. Dara Manoach at dara.manoach@mgh.harvard.edu

Results

TF-peak density distributions are heterogeneous with strong night-to-night consistency

Figure 3 compares the multitaper spectrogram [39, 40, 71, 72] and the full-night TF-peak density distribution for four control participants, illustrating the breadth of heterogeneity observed even within healthy populations. Within the distributions, we refer to the observed modes (local maxima in the density distributions) by the canonical frequency ranges. In particular, we focus on TF-peak modes in low and high sigma (σ_{slow} and σ_{fast}), which denote individualized distinctions between fast (~12–15 Hz) and slow (~10–12 Hz) spindle frequencies [73], as well as on TF-peaks modes in low-alpha (α_{low}) (7–10 Hz) and theta (θ) (4–6

Hz)—transient phenomena not previously associated with NREM sleep. These four participants exhibit variations on the four modes, which show individualized differences in mode frequency, magnitude (or absence), and bandwidth.

In contrast to the interparticipant variability, these distributions show nearly identical mode structures between nights (night 1, black curve, night 2, and gray curve), which is consistent with similar findings using spectral power [73], as well as with studies demonstrating the heritability of certain spindle features [22, 74]. Moreover, the aggregate histograms of other peak features (duration, bandwidth, etc.) are likewise consistent across electrodes and nights (Supplementary Figure S1), with no significant participant-channel-feature differences found (all KS-test, $p \gg 0.01$). The aggregate TF-peak frequency structure thus appears to be a stable and possibly trait-like phenomenon—widely heterogeneous across participants, but strongly consistent across consecutive nights for individuals—and hence a possible target for identifying different phenotypes of sleep EEG activity. However, these aggregate analyses collapse TF-peaks activity across brain state and time, ignoring important information contained in dynamics. To improve the characterization, we expand the dimensionality into continuums of sleep-depth and phase coupling.

Characterizing TF-peak ultradian and phase coupling dynamics

The SO-power histogram characterizes TF-peaks as a function of sleep depth

Sleep is a continuous and time-varying process, the oscillatory dynamics of which can be readily observed in the TF domain [40, 53, 75–77] (Figure 3). It is therefore important to tease out the effect of brain state from the complex temporal evolution of activity during sleep. Additionally, we would like to increase the state resolution of the analysis of NREM sleep, which is discretized into three stages. To do so, we compute the two-dimensional SO-power histograms (see Methods section), which represent the frequency rate-histogram as a function of SO-power, a long-established correlate of depth-of-sleep [60, 62, 63, 78], particularly for NREM in which spindles occur [6].

Figure 4 illustrates the construction of the SO-power histogram for the participant from Figure 3B, using data from electrode C3. The spectrogram (Figure 4A) is used to extract TF-peaks over the course of the night (Figure 4B, upper), the structure of which is reflected in the SO-power (Figure 4B, lower, black). The SO-power spectrogram shows the TF-peak density as a function of frequency and SO-power (Figure 4C). Each column of the SO-power histogram represents the TF-peak density across frequency (Figure 4D, upper) and each row represents the density across depth-of-sleep (Figure 4D, lower). Rows and columns can be integrated to estimate the density over a frequency range or depth-of-sleep, respectively. The SO-power spectrogram provides an improved characterization of TF-peak activity in terms of a continuum of sleep depth. Instead of the merged double peak observed in the aggregate histogram (Figure 3B), we now see two well-separated 2D modes: a σ_{fast} -mode centered at ~13 Hz between 30%–60% SO-power, and a σ_{slow} -mode centered at ~11.5 Hz between 65%–100% SO-power. The SO-power histogram thus provides a comprehensive representation of a broad range of TF-peak activity over the continuum of sleep, providing greater separability between TF-peak classes. Figure 4E shows the SO-power histogram computed for REM and NREM stages 1–3, illustrating the continuum of TF-peak dynamics that exists within discrete stages and is lost

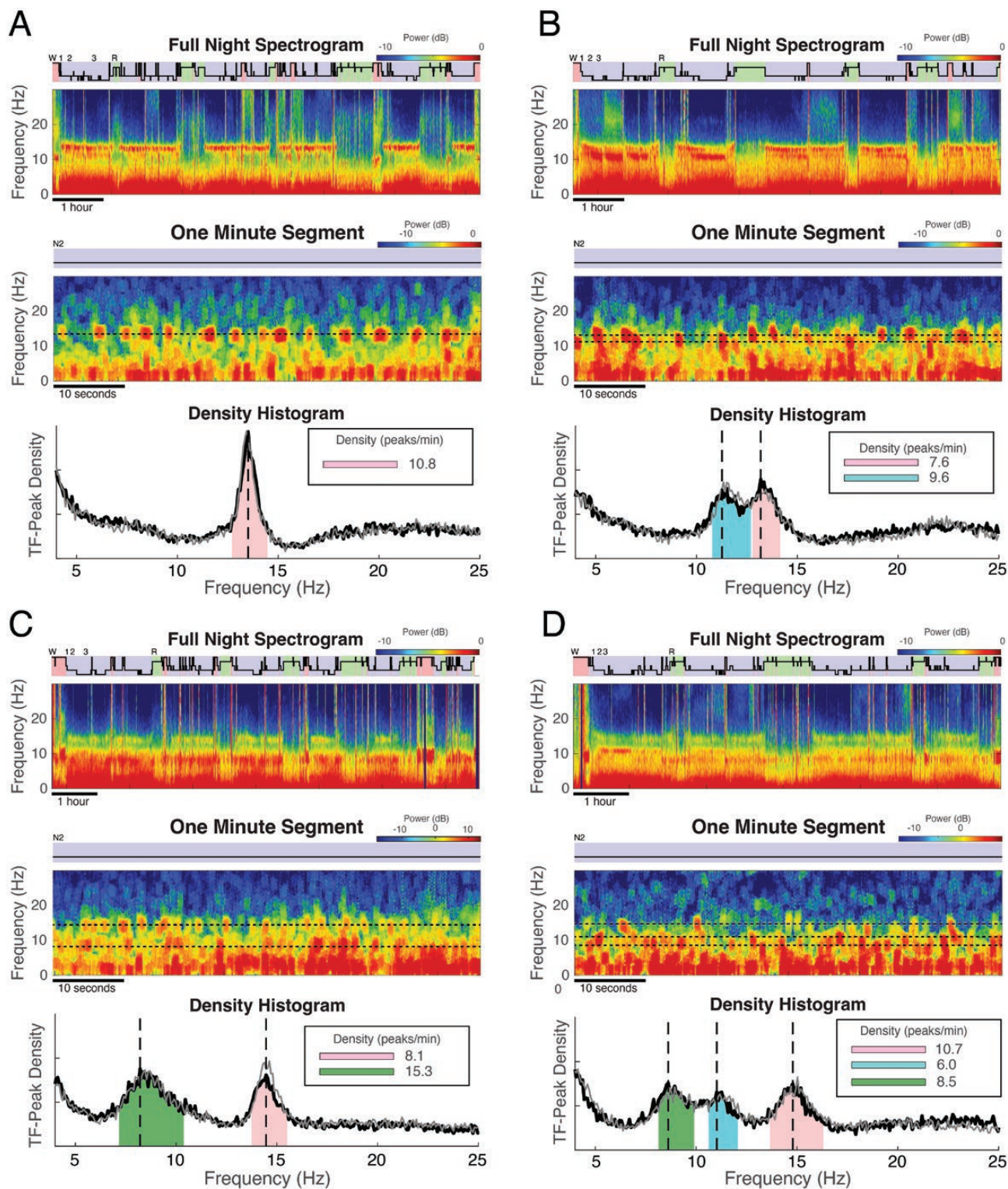


Figure 3. Healthy participants show vast heterogeneity in spectral and time-frequency peak density distribution structure. For four different participants (A–D) we show full-night (top panels) and 1-minute (middle panels) segments of the sleep EEG multitaper spectrograms for the second experimental night. We then compute the density histograms (bottom panels) for the first (thin gray curves) and second (thick black curves) nights. Each major mode in the peak frequency distribution is integrated (shaded regions) to estimate the associated density. These histograms show varied structures with various combinations of TF-peak modes, the central frequencies of which correspond directly to the transient oscillations observed in the 1-minute spectrogram segments (horizontal dashed lines, middle panels, vertical dashed lines, and bottom panels). Moreover, while the density distribution structure varies highly between participants, the first and second nights are nearly identical, showing trait-like consistency within participants.

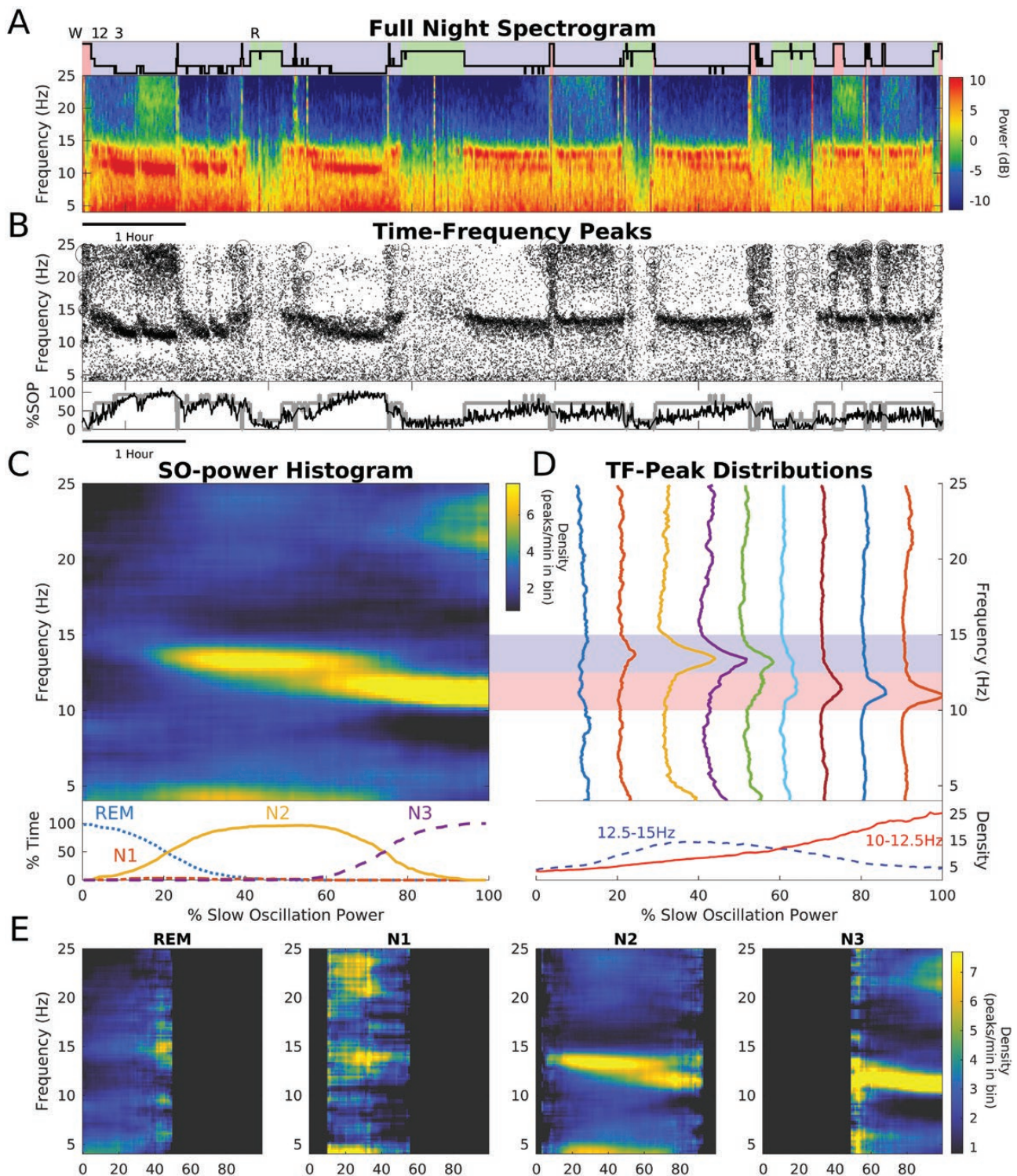


Figure 4. Time-frequency peaks (TF-peaks) exhibit stereotyped dynamics over the course of the night. We illustrate these dynamics using the participant from Figure 3B. The (A) hypnogram and EEG spectrogram along with the (B) TF-peak scatter plot (x = time; y = frequency; size = peak magnitude) and corresponding percent slow oscillation power (% SO-power) are shown. SO-power acts as a continuous-valued metric of sleep depth (black curve), which inversely mirrors the structure of the hypnogram (gray curve). (C) The SO-power histogram visualizes TF-peak density as a function of % SO-power. The percent time in the stage as a function of %SO-power (lower panel) is consistent with depth-of-sleep measured by traditional staging. (D) Columns of the SO-power histogram are the TF-peak density as a function of frequency for the corresponding %SO-power (slices at 10%–90% SO-power are shown). Rows or integrated bands of the SO-power histogram show frequency-localized TF-peak density as a function of sleep depth (10–12.5 Hz, blue, and 12.5–15 Hz, red, bands are shown). Overall, the multi-modal structure of the SO-power histogram comprehensively characterizes the dynamics of a broad range of transient oscillations during sleep, showing clear modes of activity. (E) Stage-specific SO-power histograms are shown for the same subject, illustrating the continuum of activity exists within discrete stages and may be lost due to averaging.

when averaging (see [Supplementary Figure S2](#) for the population mean). Overall, the SO-power histogram provides a substantial increase in dimensionality over traditional analyses, as well as a more robust time-frequency basis for event identification.

The SO-phase histogram characterizes TF-peak SO-phase coupling.

We can also characterize short timescale TF-peak dynamics with respect to the SO-phase. [Figure 5](#) details the construction of the SO-phase histogram for C3 from a different control participant. TF-peaks and SO-phase are extracted at each time, which can be used to make a scatter plot ([Figure 5B](#)) in which the markers are colored according to the corresponding SO-phase at the time of the TF-peak centroid. We can now observe two distinct bands of color in the scatter plot: a blue/purple band at ~14 Hz, suggesting coupling at a falling phase of the upstate between 0 and $\pi/2$, and a yellow/green band at ~9.5 Hz, suggesting coupling on the rising phase between $-\pi$ and $-\pi/2$. [Figure 5C](#) shows the corresponding SO-phase histogram, which visualizes the TF-peak density as a function of frequency and SO-phase, normalized to show the proportional density for each frequency (see Methods section). Each row is equivalent to the normalized polar histogram for the TF-peaks within that frequency bin, and bins can be integrated to examine coupling within frequency ranges ([Figure 5D](#)).

The SO-phase histogram summarizes the TF-peak SO-phase coupling structure across the entire frequency range. In this case, the SO-phase histogram structure exhibits two clear coupling modes. The first mode falls between 12 and 15 Hz with a falling phase range skewed from 0 to $\pi/2$, consistent with traditional notions of slow-wave fast spindle coupling [12, 22, 64, 65]. A second phase coupling falls between 5–10 Hz with a rising phase range from $-\pi$ to $-\pi/2$, corresponding to the low-alpha TF-peaks. This broad coupling mode is in line with findings of negative phase coupling in theta bursts [79] and in some analyses of slow spindles [73]. The SO-phase histogram thus reflects the observations from the scatter plot and traditional phase polar histograms ([Figure 5D](#)), providing a comprehensive representation of the phase coupling activity of a broad range of transient oscillations.

SO-power and SO-phase histograms provide a highly individualized, trait-like characterization of TF-peak dynamics

To better characterize general patterns of TF-peaks, we computed the SO-power and SO-phase histograms for each channel and night for all participants in the control population for all sleep epochs. [Figure 6](#) shows the SO-power and SO-phase histograms of C3 from two nights for the same four participants from [Figure 3](#). Like the aggregate density histograms, the SO-power and SO-phase histograms are highly individualized across participants yet show strong, night-to-night similarities. The heterogeneity and strong night-to-night consistency is seen broadly across control population participants and electrodes (See [Supplementary Figure S3–S6](#)), suggesting that this broader class of TF-peak activity is highly trait-like. This is also consistent with large-scale genetic studies of spindle features and their heritability [22]. Overall, this twofold SO-power/phase representation provides a robust, participant-specific, high-dimensional summary of the activity of tens of thousands of TF-peaks across different timescales in a comprehensive visualization. These results suggest that the histograms may provide an improved basis for objectively identifying distinct

EEG phenotypes based on the observed power and phase mode structure.

TF-peak topographic gradients

[Figure 7](#) shows the mean SO-power (A) and SO-phase (B) histograms over all control participants for the second (post-adaptation) night for each electrode, in which topographic differences can be observed. Results are shown for one hemisphere, given that no salient hemispherical differences were observed for either power or phase ([Supplementary Figure S7](#)).

Topographic gradients in the SO-power histogram

For the SO-power histograms across the electrodes ([Figure 7A](#)), we observe four primary modes at the following frequencies: σ_{fast} (~12–15 Hz) corresponding to traditional fast spindles, σ_{slow} (~10–12 Hz) corresponding to slow spindles, α_{low} (7–10 Hz), and θ (4–6 Hz).

The mean σ_{fast} -mode possesses properties consistent with fast spindles: centrally dominant with an ~15 Hz frequency. The magnitude is maximal at Pz. It also appears to decrease in frequency with increasing SO-power, eventually merging with the σ_{slow} -mode at ~12 Hz. In the central channels, the σ_{slow} -mode appears distinct, separated from the σ_{fast} at a slightly lower frequency, ~11 Hz, and only at >80% SO-power. The magnitude of the σ_{slow} -mode also appears to decrease from anterior to posterior, appearing faintly at Pz and absent occipitally.

The α_{low} -mode is diffuse in the group average and is distinctly lower in frequency and later in sleep depth from the occipital eyes-closed alpha that is expected during the early stages of sleep onset. The θ -mode bandwidth increases from ~3–5 Hz anterior to ~3–7 Hz posterior. In the occipital channels, the mode itself shifts to higher frequencies as SO-power increases. Additionally, the θ -mode arrives at increasingly higher SO-power moving occipitally (approximately 1% F, 10% C, 15% P, and 20% O). Together, these differences indicate the mode that is appearing deeper into sleep and higher in frequency along the anterior-posterior gradient. It should also be noted that θ -mode density waxes and wanes as %SO-power increases, suggesting that these TF-peaks are not simply artifacts of the long tail of increasing slow/delta EEG power during NREM sleep.

In this linked-mastoid referencing scheme, we see no salient regions of significance in the global comparison analysis across hemispheres ([Supplementary Figure S7A](#)), while regions of significance in the pair-wise electrode comparisons confirm the qualitative differences described above ([Supplementary Figure S8](#)).

Topographic gradients in the SO-phase histogram

[Figure 7B](#) shows the average over participants of the second (post-adaptation) night SO-phase histograms for each electrode, using data from all of the sleep (non-wake epochs). The average SO-phase histograms of the central channels display a band of SO-phase coupling in the sigma range extending from ~12 to 15 Hz. The phase distribution again skews from 0 toward $\pi/2$ as the frequency decreases within the band, indicating phase coupling with the slow oscillation apex and falling edge. In the frontal channels, the skew is even more pronounced, while moving occipitally, the mode reduces in magnitude, and the skew and the frequency range condense.

The other prominent band of SO-phase coupling appears in the theta-alpha range. In the frontal channels, this mode extends from 4 to 12 Hz and is centered at $-\pi$. Moving occipitally, this

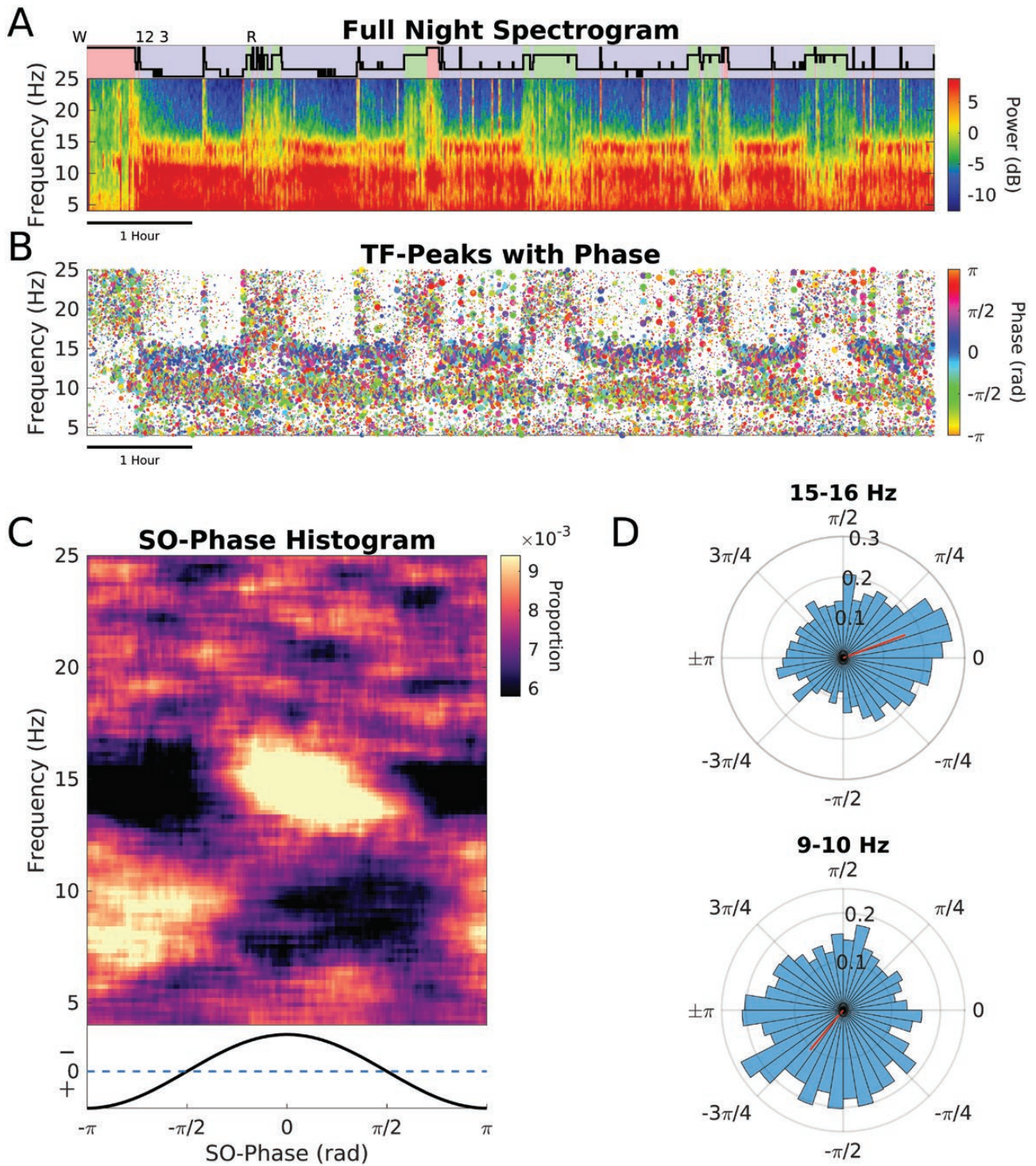


Figure 5. Time-frequency peaks exhibit stereotyped slow oscillation phase (SO-phase) coupling dynamics over a wide range of frequencies. Using a different control participant, we show the (A) hypnogram and spectrogram, as well as the (B) TF-peak, scatter plot (x = time, y = frequency, marker size = magnitude), with the color of the marker representing SO-phase at the time of the TF-peak. This plot reveals two clear bands of color, suggesting varying phase coupling at different frequencies. (C) The SO-phase histogram shows TF-peak density as a function of frequency and SO-phase, normalized row-wise to show the proportion of activity across phases for each frequency. Two clear modes of phase coupling are observed for this participant: one centered just above 0 phase and between 12 and 17 Hz and another at around $-\pi/4$ and between 6 and 11 Hz, consistent with the colors in the scatter plot. (D) Rows of the SO-phase plot can be viewed as reflecting similar information to traditional polar histograms of TF-peak activity, which are shown for bands with observed phase coupling modes. As with the SO-power histogram, the SO-phase histogram comprehensively summarizes the frequency-dependent phase coupling structure found within TF-peak activity, revealing modes of enhanced coupling activity.

mode shifts to $\sim\pi/2$ and reduces in range to 4–10 Hz. Thus, this mode shifts from the SO trough to the falling edge in an anterior–posterior gradient.

A particularly notable feature of the SO-phase histograms is that the coupling modes observed do not directly reflect the frequency ranges of the modes observed in the SO-power histogram.

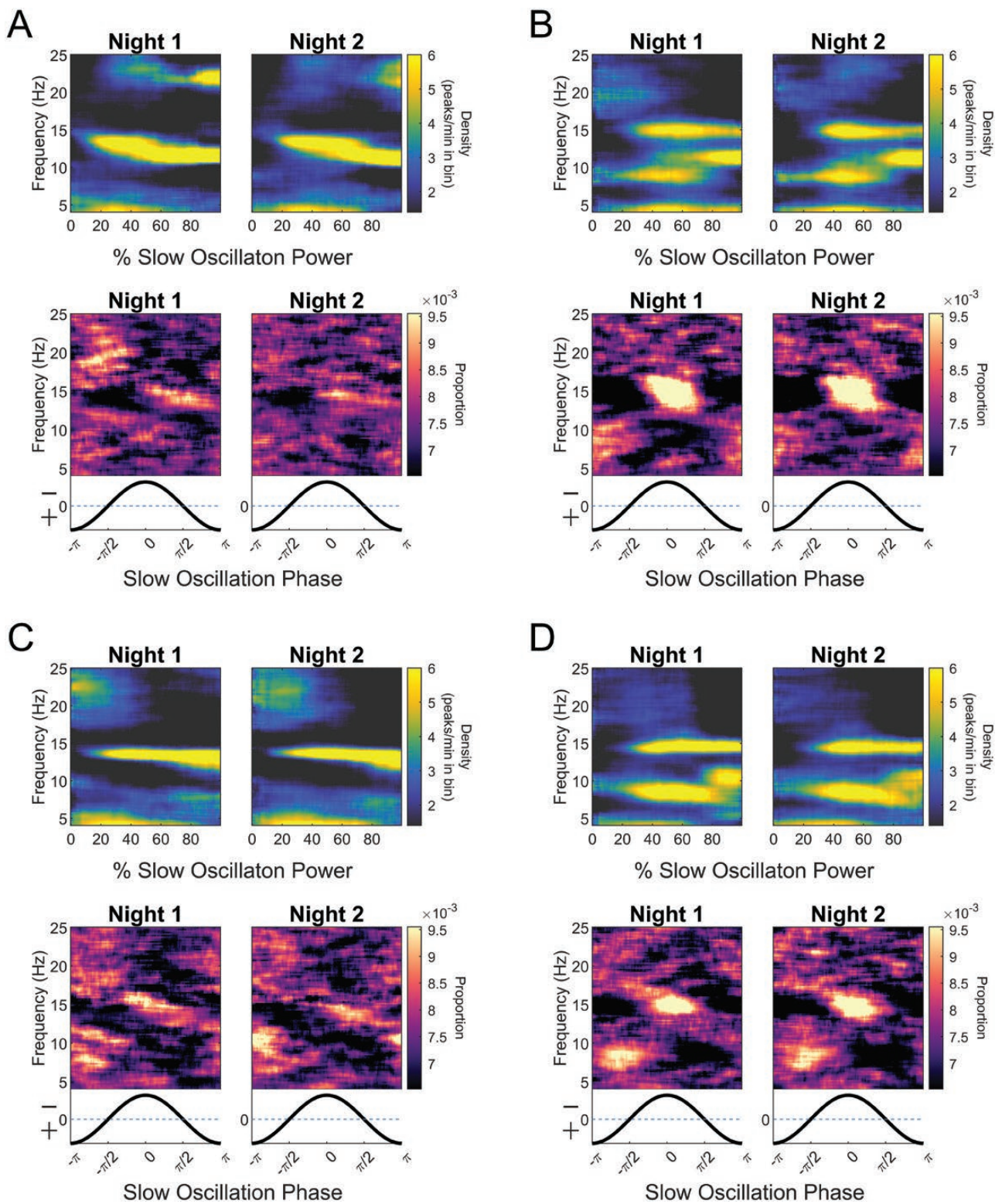


Figure 6. Together, SO-power and SO-phase histograms provide a robust EEG phenotype that differs greatly between participants yet is trait-like between participant nights. SO-power and SO-phase histograms are computed for the corresponding participants (A–D) from Figure 3, showing the data from C3 from nights 1 and 2 side by side. While each participant exhibits a distinct SO-power/phase histogram phenotypic structure, it remains highly consistent between nights within individuals.

The frequency modes of coupling tend to be more broadband than those in the SO-power and do not break into the separable narrow bands observed in the SO-power. While a lower signal-to-noise ratio may contribute to this phenomenon, these results suggest

that even in frequency ranges in which there is very little activity, the coupling of those few events may still possess phasic structure.

As with the SO-power, no salient significant hemispheric difference between corresponding channels in this reference

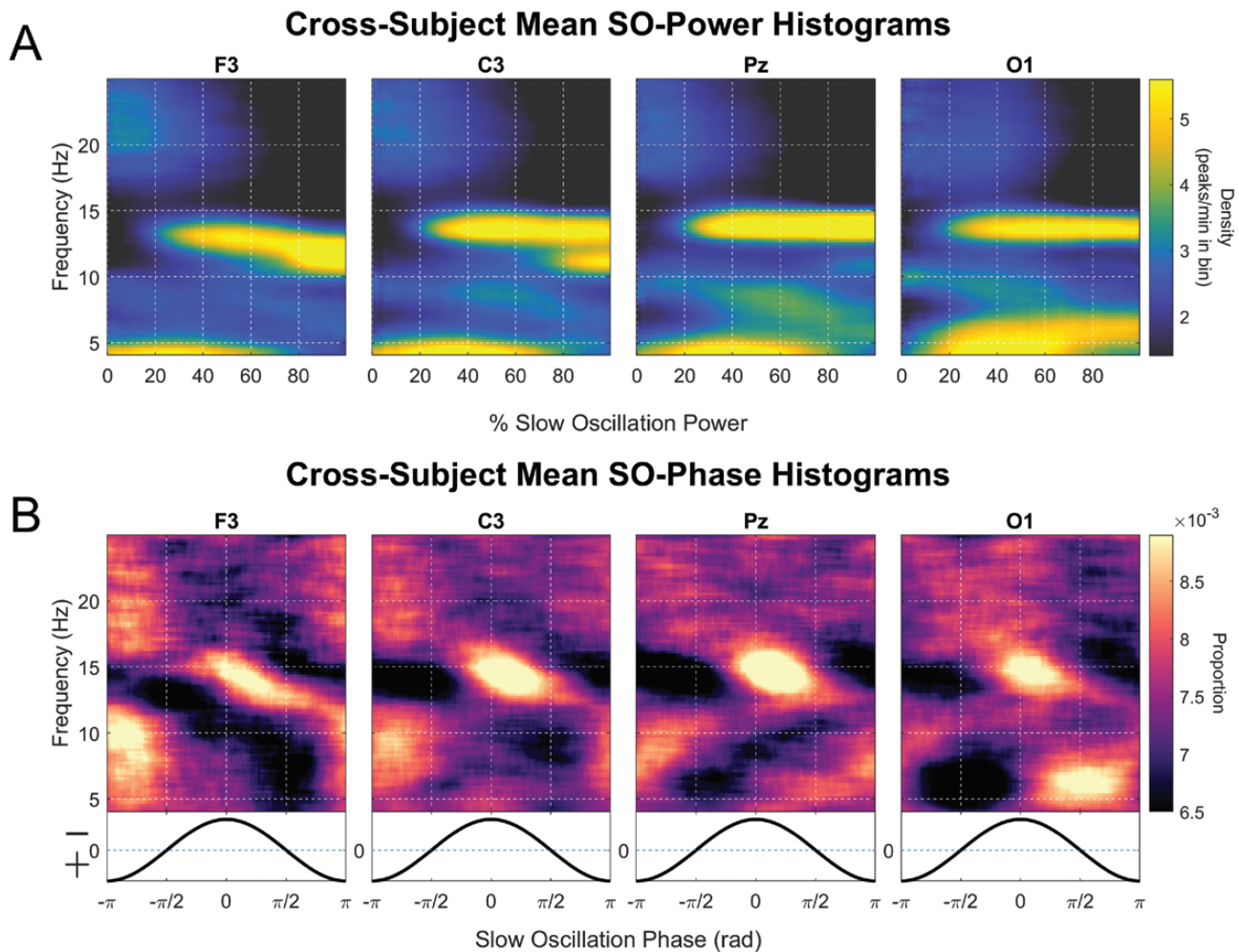


Figure 7. Population analysis of time-frequency dynamic structure shows spatial gradients of differential activity in SO-power and SO-phase histograms. The population average SO-power and SO-phase histograms were computed for each electrode using data from the second experimental night. The healthy control population average (A) SO-power histograms and (B) SO-phase histograms show spatial gradients in mode structure as a function of electrode location. Both the SO-power and SO-phase histograms suggest an oscillatory activity that differs in frequency, density, depth of sleep, and timing as a function of spatial location.

scheme was found (Supplementary Figure S7B), while marked regions of significant differences are observed between different spatial locations (Supplementary Figure S8), which agree with the qualitative differences described above.

Clinical application example: SO-power histograms suggest new SZ biomarkers

We can now leverage this expanded characterization of TF-peak activity to explore differences between populations. Figure 8 shows a comparison between the TF-peak density SO histograms in HC and medicated participants with SZ for C3 on night 2. Significantly reduced spindle activity has been observed in chronic medicated patients with SZ, as well as in antipsychotic naïve patients with early course SZ and their first-degree nonpsychotic relatives—even when exhibiting normal sleep quality and architecture [11, 16, 80, 81]. Thus, reduced activity in traditionally detected spindles has been proven important as a SZ biomarker and also a target for intervention to improve sleep-dependent memory consolidation [10–15, 74, 82]. Here we extend the analysis of group differences to TF-peak modes. Like the HCs, the SZ participants show marked intersubject differences and night-to-night consistency in the SO-power and SO-phase histograms (Supplementary Figures

S9–S12, SZ spatial distributions in Supplementary Figures S13 and S14) A comparison of the cross-participant C3 mean SO-power histograms for HC and SZ cohorts (Figure 8A) reveals differences in TF-peak dynamic structure. As expected, the SZ mean SO-power histogram shows a reduced σ_{fast} density mode, however, we also observe that the SZ mean has a broader σ_{slow} mode that extends into lighter sleep (~40% SO-power), a more prominent α_{low} mode, and a weaker θ mode. To quantify these differences, we computed TF-peak density for frequency \times SO-power regions representing σ_{fast} , σ_{slow} , α_{low} , and θ modes (boxes) in the SO-power histogram. The results show significant decrease in density for σ_{fast} [$t(34) = 4.265$, $p = .0002$] and θ modes [$t(34) = 3.030$, $p = .0046$], as well as a significant increase in density for α_{low} [$t(34) = -2.164$, $p = .037$] for patients with SZ (Figure 8B). The reduction in θ -mode density is consistent with recent findings (which used the data in the present study as one of several replication sets) of reduced theta spectral power in SZ patients [16]. No phase-based differences were observed (Supplementary Figure S15), which is in line with previous studies [12]. These previously unexplored classes of transient oscillation activity therefore provide new targets for future studies exploring an enhanced understanding of SZ and antipsychotic drugs, as well as suggesting potential novel EEG biomarkers.

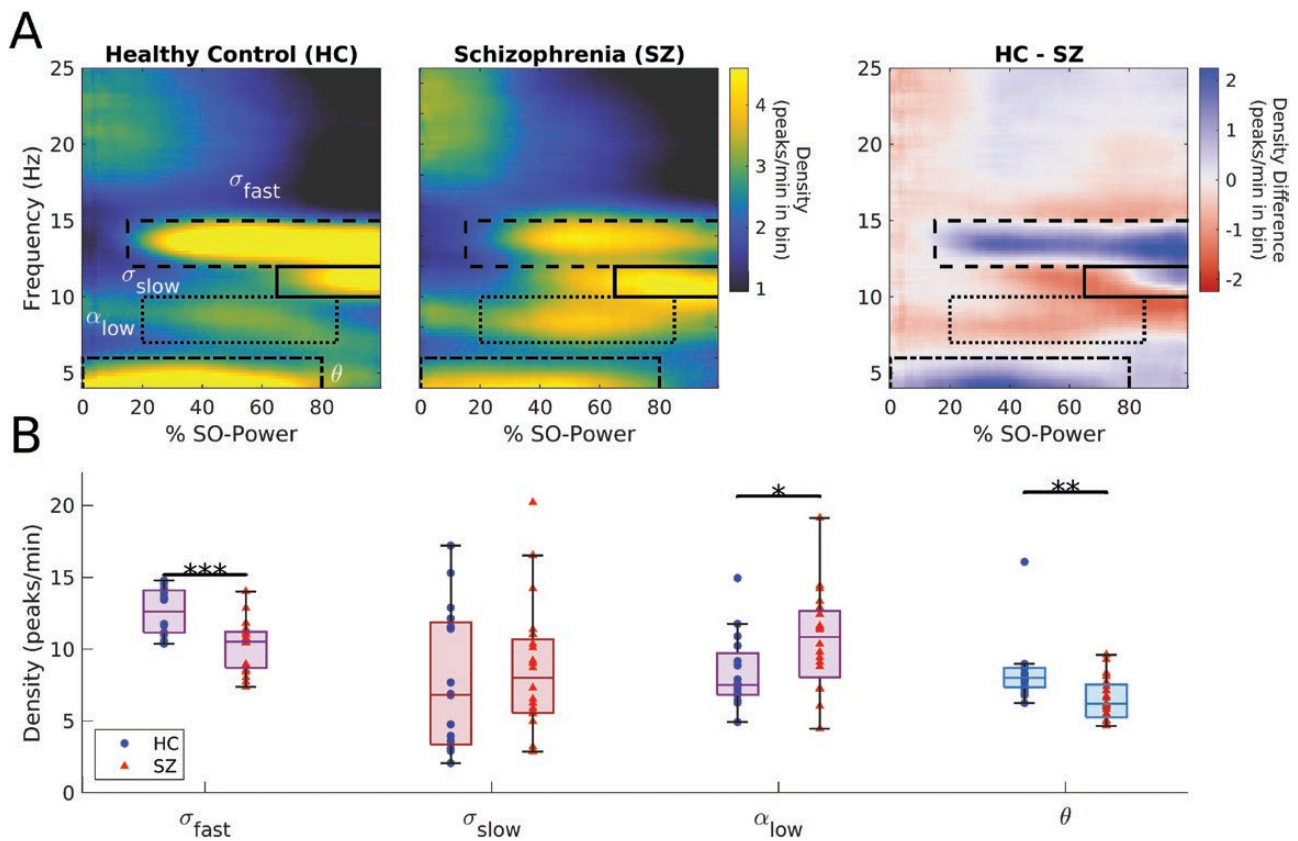


Figure 8. SO-Power histograms reveal novel significant differences in TF-peak dynamics between healthy controls (HC) and medicated patients with schizophrenia (SZ). (A) The mean SO-power (left two panels) histograms for electrode C3 for night 2 are shown for controls and medicated patients with schizophrenia, along with the corresponding difference (right panel). In the difference histogram, power regions in which control participants had a larger mean density are shown with red triangles, and those in which SZ patients have a larger mean density are shown with blue circles. Informed by the previous analyses of SO-power histograms in the healthy controls, regions of interest were created for σ_{fast} , σ_{slow} , α_{low} , and θ modes (boxes), and the corresponding densities were computed for all HC and SZ cohorts. (B) shows the HC and SZ distributions of the densities in the ROIs with significance (t-test, $*p < .05$, $**p < .01$, $***p < .001$), showing significance for σ_{fast} , α_{low} , and θ . The results in sigma agree with previous analyses of spindle deficits in SZ patients. Moreover, these results show that SZ patients have a significant increase in TF-peak density in α_{low} and a significant decrease in θ . These previously unexplored frequencies of transient oscillation activity, therefore, provide novel additional information for improving our mechanistic understanding of SZ, as well as for developing novel EEG biomarkers.

Discussion

Transient oscillations are well-represented by TF-peaks identified on spectrograms. The spatial-temporal dynamics of transient oscillations can be easily identified with property distributions, which can be efficiently summarized in SO-power and SO-phase histograms. Together, the SO-power and SO-phase histograms provide a comprehensive picture of TF-peak dynamics, revealing dynamics lost with discrete sleep staging and use of fixed canonical frequency bands (Supplementary Figure S2). While this approach greatly increases the dimensionality of the representation of spindle-like activity, the results confirm findings from existing studies of spindle activity and cross-frequency coupling. Namely, the features of the observed mode at σ_{fast} encompass the frequency range, central spatial dominance, predominance in Stage 2 sleep, and peak phase coupling found in studies of fast spindles [7, 73, 83]. Also, the features of the mode at σ_{slow} encompass the frequency range, frontal spatial dominance, and phase coupling found in studies of slow spindles [7, 22, 25, 73, 84]. Integrated rates within these bands (Figure 3, bottom panels) are consistent with some existing spindle detection methods [27, 33, 34, 85]. Given that these results are validated using a method that does not employ spindle-only event detection affirms the overall robustness of these phenomena. Additionally, this approach provides several enhancements to our understanding of the

underlying transient oscillation phenomenology, as well as a basis for improved future methodological approaches.

TF-peak heterogeneity demonstrates neurodiversity in healthy sleep EEG

These analyses vividly reveal heterogeneity among healthy participants of a scope and magnitude far beyond that which is accounted for in traditional studies (Figures 2 and 5). We must therefore expand the notion of “normal” sleep EEG activity to account for this neurofunctional diversity. Previous studies have described high participant-to-participant variability in spindle oscillatory properties, including waveform spindle morphology and frequency [22, 73, 84]. Our results extend beyond morphological variability to show that even across healthy participants, TF-peak modes can vary dramatically in number, frequency, magnitude, and timing in the ultradian cycle. From a clinical perspective, this means that there exists a wider gradient of phenotypes in the phenomenology of normal or healthy sleep for which we must account. That is, there exist healthy people with and without significant activity in σ_{slow} , α_{low} , etc., such that even dramatic differences in TF-peak distribution may not necessarily constitute pathological activity. Future clinical guidelines should explicitly characterize this broad neurodiversity to avoid bias in clinical diagnostics. Given the demonstrated heritability of spindle activity and morphological features [22], future studies can examine

the genetic associations with components of TF-peak dynamical structure. From an analysis standpoint, these findings suggest that TF-peak mode heterogeneity is likely a major source of variability in existing spindle studies, especially those with small numbers of subjects. Thus, it will be important to understand the distribution of naturally occurring phenotypes in future studies in order to properly construct normative distributions.

Phase-coupling can occur at frequencies of low TF-peak density

Perhaps surprisingly, we observe that the frequencies at which TF-peaks have structured SO-phase coupling do not necessarily correspond to the frequencies at which they have high density. That is, the phase-coupling modes observed in the SO-phase histograms tend to be broad and encompass frequency ranges larger than those observed in SO-power histograms. For example, the mean population SO-power histogram in C3 (Figure 7A) shows a narrow 13–14 Hz σ_{fast} mode, yet the SO-phase histogram has a broader 12–17 Hz mode extending above where TF-peak activity occurs with high density. Coupling outside of the σ_{fast} mode range is seen broadly across all participants and electrodes (Supplementary Figures S3–S6). Similarly, the 4–12 Hz phase coupling mode does not clearly delineate the frequency range of any of the other density modes. These results suggest that there exist frequencies in which there may be a minimal activity, yet the timing of that activity may be coupled to a specific SO-phase. The SO-phase timing of TF-peaks thus appears to be an intrinsic property linked to oscillation frequency, which does not necessarily correspond only to the regions of high density. Frequency/phase relationships like this are consistent with mathematical models of coupled oscillators [86] or of mechanistic scenarios in which different phases of SO facilitate communication at different frequencies. Given the skew observed in the 12–17 Hz SO-phase modes (Figure 7B), an alteration in TF-peak frequency would correspond to a phase shift with respect to the SO. This linkage could suggest disease models in which pathological changes in TF-peak frequency result in shifted phase preference. For example, this may provide a potential mechanism relating age-related changes in spindle frequency [23] with the phase shift observed in aging spindles [5, 18], as well as the observed variability in slow-wave spindle coupling [87].

Additional classes of spindle-like transient oscillations

Consistent findings of TF-peak density modes at α_{low} and θ modes across subjects suggest that these are two additional classes of potentially important transient oscillations to be investigated—both in terms of being an example of spindle-like activity, as well as for their potential utility in biomarker identification as evidenced in the SZ analyses. Visualization of the raw spectrogram shows that there are salient TF-peaks occurring at these frequencies (e.g. Figure 3). Moreover, the SO-power histogram density structure at these frequencies is distinctly modal and not monotonically increasing as a function of %SO-power, which shows that they are not simply artifacts of the long tail of delta as slow-wave sleep progresses. There is known sleep EEG activity in these frequency ranges. In addition to general observations of alpha incursion into NREM (e.g. arousals and alpha-delta sleep), which is typically viewed as pathological [88–94], alpha has been observed in healthy populations across all stages of sleep [88]. In particular, peri-REM alpha transient bursting has been shown to occur at lower alpha frequencies [40, 95], and alpha micro-states

have been observed during NREM [96–98]. However, new insights from our analysis show that α_{low} TF-peaks during NREM (e.g. Figures 2 and 5C and D) appear to be a common, spindle-like trait within the healthy population, possessing robust time-frequency structure and SO-phase-coupling properties. There is also precedent for theta-range transient activity, which has been observed intracranially as hippocampal epileptiform waveforms [99], and 5–8 Hz transient bursts have been shown to occur prior to cortical down states in epileptic patients and rodents [79, 100]. Further analysis of these TF-peak modes will help to elucidate their function in both healthy and pathological sleep, as well as their potential utility as biomarkers.

Improved characterization for TF-peak classes in higher dimensions

The composition of the power and phase histograms indicate that TF-peak modes can exhibit a topographical gradient across multiple dimensions. That is, in different parts of the brain, transient oscillatory activity can vary in power, frequency, timing in the ultradian cycle, and in the SO-phase coupling structure. These findings enable substantially improved characterization of groups of related TF-peaks based on multiple dimensions, providing greater separation between classes. For example, the use of depth-of-sleep can greatly facilitate the definition of fast and slow spindles, which are currently categorized using a fixed (e.g. 12 Hz) or individualized [73] frequency cutoff. Given the substantial overlap between fast/slow frequency modes (e.g. Figure 3B and D), there is no clear separation by frequency alone. By adding depth of sleep (%SO-power) as a dimension, we now have two clearly separable modes (Figures 3 and 6). Ultimately, we can describe events in the SO-power \times SO-phase \times frequency space (Supplementary Video, Supplementary Figures S16 and S17) and beyond, providing an improved framework for automated identification and for characterizing the functional differences between classes of TF-peaks.

Toward a sleep continuum

The dynamics observed across the SO-power histogram within single scored stages, most notably within NREM, highlight the degree to which a continuum of sleep dynamics still exist within fixed scored stages (Figure 4E, full population results in Supplementary Figure S2). Most notably, we observe a broad continuum of changes within N2 sleep, with low and high %SO-power showing marked differences in activity with respect to the relative proportions of sigma, theta, and low-alpha density. Overall, these findings support a hypothesis that depth of NREM sleep is a continuous rather than discrete phenomenon and should be modeled as such. It will therefore be important to explore the benefits of continuous versus discrete NREM characterizations. While this study used %SO-power, other normalization approaches will be more appropriate for other applications (e.g. reducing variability in heterogenous data, separation of REM from NREM). Thus further studies will analyze the pros and cons of different continuous metrics and normalizations [48–59] across a wide array of real-world population data.

Given the need for clinical translation and relation to past studies, it will be important to also provide approaches to map continuous metrics to discrete staging. To those ends, we provide a table with the mean SO-power for each sleep stage in Appendix 3, which is computed for several different normalizations. Moving forward, approaches can be also developed to provide individualized staging bounds based on TF-peak mode structure. Ultimately, it will be worthwhile for clinicians to

consider the benefits of switching away from discrete sleep stages and towards a sleep continuum.

Extensions and future directions

Future work can extend these analyses to explore spatial activity using high-density EEG under different referencing schemes, and to look at other features using multivariate analyses. Moreover, since the method is agnostic to spectral estimators, analyses of the stability of TF-peak features across multiple estimators (multitaper, wavelet, ARMA, etc.) could indicate the most relevant, defining properties of physiologically important transient oscillations. Parameters and merge procedures can also be optimized for performance or for specific applications [101]. Furthermore, future modeling work can provide parametric models of the structure for the SO-power and phase histograms, providing a substantial dimensionality reduction of the current nonparametric forms.

Given the demonstrated variability between participants and trait-like consistency between nights, transient oscillatory activity, as characterized by SO-phase and SO-power histograms, shows promise as the basis of an electrophysiological phenotype—simultaneously encapsulating the dynamics of neural activity, phase coupling, and sleep. Ultimately, with a more complete characterization of the properties and natural variability of transient oscillations, we can more accurately understand the underlying neural mechanisms, providing improved comprehensive descriptors of neurological health and identifying potential biomarkers of disease.

Supplementary Material

Supplementary material is available at *SLEEP* online.

Funding

This work was supported by the National Institute of Neurological Disorders and Stroke under grant R01NS096177 (MJP) and the National Institute of Aging R01AG054081 (MJP).

Acknowledgments

The authors would like to thank Dimitrios Mylonas for providing helpful guidance on study data as well as facilitating data transfer.

Disclosure Statement

Financial disclosure: None.

Nonfinancial disclosure: None.

Appendix 1: TF-Peak Identification

We computed multitaper spectrograms [40, 72] for each EEG channel using a data window of 1 s, with 0.05-second step size, a time-half-bandwidth of 2, and 3 tapers, to provide a spectral resolution of 4 Hz. Analysis was thus restricted to a frequency range of 4–25 Hz to reduce any spectral leakage slow components. Zero padding of 2^{10} data points per window were used to provide an interpolation sufficient to compute smooth peak structure. These parameters were chosen with the goal of optimizing the temporal/frequency resolution tradeoff in TF-peak detection, and corresponding with results from Dimitrov et al. [34] in which

TF-peaks have been shown to provide a more robust characterization of spindle-like activity than traditional spindle detection. While certain features such as TF-peak bandwidth and duration may be sensitive to spectral estimator and choice of parameters, the topographical centroid (from which TF-peak timing and frequency are derived) is generally robust to spectral estimator and parameters. See Prerau et al. [40] for a detailed discussion of multitaper spectral estimation, principled parameter selection, and sleep EEG spectrogram dynamics. Spectrograms are displayed in dB unless otherwise noted in the color axis. Analysis was limited to a maximum of 5 min before and after the first and last epochs of scored sleep. For records with significant initial/terminal artifact periods, fragmented experimental starts, or scoring issues, start, and end times were adjusted manually.

The EEG power spectrum is comprised of both oscillatory and non-oscillatory components. Oscillatory spectral peaks sit on top of a non-oscillatory component, generally characterized by a $1/f^\alpha$ function. If this non-oscillatory component is not removed, peak properties such as height and frequency must be computed relative to the tangent of the $1/f^\alpha$ curve. To simplify this computation, we normalize (division in raw power units) the spectrogram by a baseline prior to input to the watershed algorithm. The baseline spectrogram is estimated as the second percentile across time for each frequency bin of artifact-rejected data. This value was chosen to be a highly conservative estimate of the lower bounds of the $1/f$ background EEG structure across the night—providing some whitening of the spectrum with minimal disturbance of peak structure. As the non-oscillatory structure is known to change dynamically during sleep [58, 102], future iterations of this algorithm may compute the baseline using dynamic state-space modeling methods for $1/f^\alpha$ and peak estimation [76]. However, this process is currently computationally intensive and would add significantly to processing time.

Our approach to identifying TF-peaks in the spectrogram is based on the watershed [44–46], which is commonly used for image segmentation in computer vision applications. The watershed method treats an image as topography and identifies the catchment basins, that is, the troughs, into which water falling on the terrain would collect. For this study, we apply the MATLAB implementation of the watershed, *watershed* [103], to the negative of the baseline-normalized spectrogram in raw power units (not dB), thus identifying the local maxima and their surrounding regions. To reduce the over-segmentation of local maxima, the standard practice is for neighboring regions to be merged using a rule based on the specific needs of the application [44–46]. Here, for identifying transient oscillations, we developed a novel merge rule designed to form complete, distinct peaks in the spectrogram topography. By using the watershed as the basis for peak detection, we provide additional flexibility over previous methods [41–43, 47], which are based on parametric models of spectra or the spectrogram. For computational efficiency, we perform this procedure in parallel on 1-minute segments of the spectrogram.

Here, we propose a novel merge rule designed to form large, complete peaks—that is, peaks with a large height relative to the base and surrounding boundary points of similar heights—but without overly merging distinct peaks. For this rule, we computed a weight between each watershed region and its neighbors, with a higher weight indicating a higher priority for merging.

For a given watershed region i , let B_i be the heights of the pixels at the boundary between i and all surrounding regions, and let $A_{i,j}$ be the heights at the adjoining boundary between region i and neighbor j . The merge weight between the two regions, $w_{i,j}$, is based on two factors: $C_{i,j}$ and $D_{i,j}$, which are shown in Figure 9.

When a peak is complete, we expect the boundary to be at similar heights all around, so we compute the difference between the maximum of the adjoining boundary pixels between the regions i and j the overall minimum boundary point of the region i :

$$C_{i,j} = \max(A_{i,j}) - \min(B_i)$$

The second factor relates to how distinct neighboring regions are from each other, and is the difference between the maximum height of j , j_{\max} , and the maximum of the adjoining boundary:

$$D_{i,j} = j_{\max} - \max(A_{i,j})$$

The overall directed weight, or importance to merge the region j into i , $w_{i,j}$ is the difference between these factors:

$$w_{i,j} = C_{i,j} - D_{i,j}$$

Merging based on this weighting is specifically intended to prevent instances of large, contiguous peaks being fractured between two local maxima. The topographical components involved in the merge weights are illustrated in Figure 9. In the general case (Figure 9A), the difference between $C_{i,j}$ and $D_{i,j}$ is indicative of the degree of separation and completeness of the two regions. When a single peak is fractured (Figure 9B, left), $D_{i,j}$ will tend to 0, leading to a high weight. When peaks are separate (Figure 9B, right), $C_{i,j}$ will tend to 0, leading to a low weight.

Following the initial watershed, the weights of all neighboring regions are computed. In an iterative manner, the regions corresponding to the largest weight are merged according to the corresponding direction. Any affected edge weights are then updated. This process continues until the largest weight is below a set threshold value. We use a threshold value of 8 based on preliminary empirical tests, but segmentation is qualitatively similar over a range of surrounding values. In practice, this acts as a hyperparameter value that should be evaluated for each data set. Future work will explore means of optimizing the threshold value as well as possible

alternative merge rules. Results are illustrated in Supplementary Figure S18.

Given the properties of the watershed, our algorithm applied to a solitary peak on a flat surface will determine that the peak boundaries extend indefinitely, as there will be no other peaks to segment. To compensate for such peaks, as well as for the possibility of over-merging low-lying neighbors, both of which misrepresent the extents of the peaks, we define a volume-concentrated boundary, which contains 80% peak volume and trims each region to this boundary. The boundary is identified by intersecting the peak topography with a plane such that the resulting boundary contains $\leq 80\%$ of the original peak volume.

The vast majority of the obtained peaks are un-merged local maxima, with small duration, bandwidth, and prominence, and thus likely to be noise. For the present analyses, we use the time and frequency resolutions of the spectrograms—the half-window length (0.5 s) and half-bandwidth (2 Hz), as lower cutoffs. While future work may characterize the distribution of noise peaks, this conservative measure of data reduction makes no a priori assumption on noise structure, only on what peaks the spectral estimator could plausibly resolve given the spectral resolution. In setting a conservative approach to noise removal, we aim to minimize any signal that is removed, with the goal that analysis of the aggregate distributions will reveal global structure in the presence of any residual noise. Additionally, TF-peaks with a frequency below 4 Hz were not considered in the analysis, as the 4 Hz, spectral resolution means they cannot be disambiguated from the SO itself and are likely biased due to the variability of the baseline at low frequencies. On average $\sim 2\%$ of peaks remained after noise reduction, which is reasonable given the way the watershed identifies all local maxima, however small (see Supplementary Figure S18H). TF-peaks during scored wake epochs were also removed, unless stated otherwise.

For each participant, channel, and night, we compute the time and central frequency of each TF-peak using the peaks topographical weighted centroid. SO-power and phase (see Appendix 2), and sleep stage are determined for each peak based on the interpolated value at the peak time. In addition, it is possible to compute additional features, such as TF-peak bandwidth, duration, area, prominence, maximum spectral power, and volume, though these are not examined in detail in this set of analyses.

Appendix 2: SO-Power and SO-Phase Histogram

To estimate the slow-oscillation power (SO-power), an additional multitaper spectrogram of the EEG signal with artifact-rejected epochs was computed using 30-sec windows, 15-sec step-size, 29 tapers, and time-half bandwidth of 15. These parameters were selected to reflect the 30 s stationarity assumption in ultradian dynamics implicit in traditional sleep scoring while providing a 1 Hz spectral resolution. SO-power was computed by integrating between 0.3 to 1.5 Hz and converting it to dB. To compare across participants and to relate to established analyses of “% slow wave amplitude” in the two-process model, the SO-power was normalized in terms of percentage of maximum (%SO-power), such that 0% and 100% SO-power corresponded to the 1st and 99th percentile of artifact-free data during sleep (non-wake) times, respectively. This normalization provides the clearest presentation for these specific data, in which all

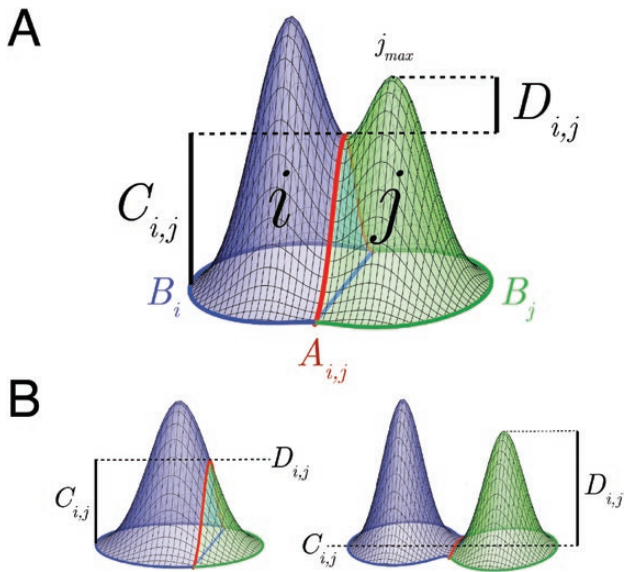


Figure 9. Schematic of the weight computation for the watershed merge rule. Given two regions i and j , we compute a directed weight for merging j into i based on two factors: (1) $C_{i,j}$, the difference between the max of the common border $A_{i,j}$ and the min of the border of the region i , B_i , and (2) $D_{i,j}$, the difference between the maximum of region j and the maximum of $A_{i,j}$. (A) These factors are indicative of the degree of separation and completeness of the two regions. (B) When a single peak is fractured (left), $D_{i,j}$ will tend to 0 leading to a high weight, and when peaks are separate (right), $C_{i,j}$ will tend to 0, leading to a low weight.

subjects reach N3 sleep, however other normalization schemes will be more appropriate for homogeneous populations and data sets. We demonstrate the robustness of our analyses to other normalization schemes (alignment to 5th percentile, the proportion of total power in the SO range, etc.) and with unnormalized data, which is reported in [Supplementary Figures S18 and S20](#).

To estimate the slow-oscillation phase (SO-phase), the EEG time-domain signal was band passed from 0.3 to 1.5 Hz using a zero-phase filter approach. The filtered signal was Hilbert transformed. TF-peak phase was computed using interpolation of the unwrapped Hilbert phase at the TF-peak times. TF-peak phase was then re-wrapped such that a phase of 0 rad corresponds to the “peak” of the SO with respect to surface negative EEG, while a phase of π or $-\pi$ rad corresponds to the “trough.”

The generalized construction is summarized as follows:

Construction of TF-Peak Feature Histograms

Given P , a set of TF-peaks with a frequency and time, a feature signal (such as SO-power or SO-phase) S_t , and a set of M feature bins and N frequency bins

1. Define a $N \times M$ feature histogram, $FS_{n,m}$
2. For each feature bin, m
 - 2.1. Find all times at which the signal S_t falls within the given feature bin
 - 2.2. Compute the total time T_m for which S_t fell within that bin
 - 2.3. For each frequency bin, n :
 - 2.3.1. Define the rate within the feature spectrogram, $FS_{n,m} = |P_{n,m}|/T_m$, where $P_{n,m} \subseteq P$ that falls into both the frequency and feature bin
3. For phase histograms, normalize each row across frequency such that $\sum_{n=1}^N FS_{n,m} = 1$

In this analysis, for both power and phase histograms we used a 1 Hz frequency bin width with a 0.2 Hz step size. For the SO-power histogram, we used a SO-power bin width of 20% with a 1% step size. For the SO-phase histogram, we used a $2\pi/5$ bin width with a $2\pi/100$ step size. This yielded power and phase histograms with the same dimensions.

Additionally, it is possible to explore the TF-peaks as a function of both phase and depth of sleep by forming three-dimensional TF-peak histograms using discrete frequency \times SO-power \times SO-phase bins. For each SO-power bin, the frequency-SO-phase histogram slice is separately normalized as above, giving the distribution of SO-phase, conditional on frequency, and SO-power. The resulting depth-of-sleep dynamics can be visualized as an animation or as two-dimensional slices from the three-dimensional histogram.

Appendix 3: Slow Oscillation Feature Distribution in Scored Stages

To facilitate translation between existing approaches with fixed sleep stages and the continuous metrics reported in this paper, [Table 1](#) provides a summary of the HC population mean \pm standard deviation of several continuous slow oscillation (SO) metrics: % SO-power, SO-power aligned at each participant’s 5th nightly percentile, proportion SO-power (the ratio of SO [0.3–1.5 Hz] to total [0.3–40 Hz] power), unnormalized power in dB. Statistics were computed from the experimental night (night 2) for all healthy participants. Wake is omitted, as it is not a unitary state. Thus, variability due to combinations of quiescent, non-quiescent, eyes open/closed conditions produces a multi-modal and long-tailed distribution, requiring further analysis or state segmentation in subsequent studies. Additionally, distribution of % time in stage across these normalizations is shown for the wake and all sleep stages in [Supplementary Figure S20](#). Note that caution must be exercised before applying any generalizations of these results to more homogeneous datasets or when using EEG data with different referencing schemes.

Table 1. Means \pm standard deviations of slow oscillation power for each electrode (column), normalization method (row), and sleep stage (sub-row) for night 2 of all healthy control subject data

| | | F3 | C3 | Pz | O1 |
|-----------------------------|-----|-----------------|-----------------|-----------------|-----------------|
| % SO-power | REM | 25 \pm 15 | 22 \pm 11 | 21 \pm 10 | 25 \pm 21 |
| | N1 | 30 \pm 20 | 29 \pm 17 | 29 \pm 15 | 31 \pm 15 |
| | N2 | 50 \pm 19 | 50 \pm 18 | 49 \pm 17 | 46 \pm 16 |
| | N3 | 85 \pm 9 | 87 \pm 9 | 88 \pm 9 | 85 \pm 9 |
| 5th Percentile aligned (dB) | REM | 3.2 \pm 2.8 | 2.6 \pm 2.1 | 2.4 \pm 1.9 | 3.1 \pm 2.1 |
| | N1 | 4.1 \pm 3.7 | 4.0 \pm 3.2 | 3.9 \pm 2.9 | 4.2 \pm 2.7 |
| | N2 | 7.9 \pm 3.6 | 7.9 \pm 3.3 | 7.6 \pm 3.2 | 7.1 \pm 3.1 |
| | N3 | 14.4 \pm 1.6 | 15.0 \pm 1.7 | 15.1 \pm 1.6 | 14.2 \pm 1.7 |
| Proportional power | REM | 0.44 \pm 0.13 | 0.38 \pm 0.10 | 0.37 \pm 0.08 | 0.40 \pm 0.09 |
| | N1 | 0.45 \pm 0.13 | 0.39 \pm 0.11 | 0.38 \pm 0.11 | 0.38 \pm 0.12 |
| | N2 | 0.54 \pm 0.13 | 0.49 \pm 0.13 | 0.47 \pm 0.13 | 0.46 \pm 0.14 |
| | N3 | 0.71 \pm 0.06 | 0.71 \pm 0.06 | 0.72 \pm 0.06 | 0.72 \pm 0.07 |
| Absolute (dB) | REM | 15.4 \pm 2.8 | 13.4 \pm 2.1 | 13.1 \pm 1.9 | 10.8 \pm 2.1 |
| | N1 | 16.3 \pm 3.7 | 14.6 \pm 3.2 | 14.6 \pm 2.9 | 11.8 \pm 2.7 |
| | N2 | 20.0 \pm 3.6 | 18.8 \pm 3.3 | 18.3 \pm 3.2 | 14.8 \pm 3.1 |
| | N3 | 26.6 \pm 1.6 | 25.9 \pm 1.7 | 25.7 \pm 1.6 | 21.9 \pm 1.7 |

References

1. Stone JL, et al. Early history of electroencephalography and establishment of the American Clinical Neurophysiology Society. *J Clin Neurophysiol.* 2013;**30**(1):28–44. doi:[10.1097/WNP.0b013e31827edb2d](https://doi.org/10.1097/WNP.0b013e31827edb2d).
2. Berger H. Über das elektrenkephalogramm des menschen. *Archiv f Psychiatrie.* 1929;**87**(1):527–570. doi:[10.1007/BF01797193](https://doi.org/10.1007/BF01797193).
3. Fisch B. *Fisch and Spehlmann's EEG Primer: Basic Principles of Digital and Analog EEG.* 3rd ed. Amsterdam NY, USA: Elsevier; 1999:644.
4. Schomer DL, Lopes da Silva FH, eds. *Niedermeyer's Electroencephalography: Basic Principles, Clinical Applications, and Related Fields,* 7 edn (New York, NY, USA). 2017. doi:[10.1093/med/9780190228484.001.0001](https://doi.org/10.1093/med/9780190228484.001.0001).
5. Helfrich RF, et al. Old brains come uncoupled in sleep: slow wave-spindle synchrony, brain atrophy, and forgetting. *Neuron.* 2018;**97**(1):221–230.e4. doi:[10.1016/j.neuron.2017.11.020](https://doi.org/10.1016/j.neuron.2017.11.020).
6. Berry RB, Brooks R, Gamaldo CE, Harding SM, Lloyd RM, Marcus CL and Vaughn BV for the American Academy of Sleep Medicine. *The AASM Manual for the Scoring of Sleep and Associated Events: Rules, Terminology and Technical Specifications, Version 2.2.* Darien, Illinois: American Academy of Sleep Medicine, 2015. www.aasmnet.org.
7. De Gennaro L, et al. Sleep spindles: an overview. *Sleep Med Rev.* 2003;**7**(5):423–440. doi:[10.1053/smr.2002.0252](https://doi.org/10.1053/smr.2002.0252).
8. Fernandez LMJ, et al. Sleep spindles: mechanisms and functions. *Physiol Rev.* 2020;**100**(2):805–868. doi:[10.1152/physrev.00042.2018](https://doi.org/10.1152/physrev.00042.2018).
9. Fogel SM, et al. The function of the sleep spindle: a physiological index of intelligence and a mechanism for sleep-dependent memory consolidation. *Neurosci Biobehav Rev.* 2011;**35**(5):1154–1165. doi:[10.1016/j.neubiorev.2010.12.003](https://doi.org/10.1016/j.neubiorev.2010.12.003).
10. Manoach DS, et al. Reduced sleep spindles in schizophrenia: a treatable endophenotype that links risk genes to impaired cognition? *Biol Psychiatry.* 2016;**80**(8):599–608. doi:[10.1016/j.biopsych.2015.10.003](https://doi.org/10.1016/j.biopsych.2015.10.003).
11. Wamsley EJ, et al. Reduced sleep spindles and spindle coherence in schizophrenia: mechanisms of impaired memory consolidation? *Biol Psychiatry.* 2012;**71**(2):154–161. doi:[10.1016/j.biopsych.2011.08.008](https://doi.org/10.1016/j.biopsych.2011.08.008).
12. Demanuele C, et al. Coordination of slow waves with sleep spindles predicts sleep-dependent memory consolidation in schizophrenia. *Sleep.* 2017;**40**(1). doi:[10.1093/sleep/zsw013](https://doi.org/10.1093/sleep/zsw013).
13. Baran B, et al. Spared and impaired sleep-dependent memory consolidation in schizophrenia. *Schizophr Res.* 2018;**199**:83–89. doi:[10.1016/j.schres.2018.04.019](https://doi.org/10.1016/j.schres.2018.04.019).
14. Manoach DS, et al. Abnormal sleep spindles, memory consolidation, and schizophrenia. *Annu Rev Clin Psychol.* 2019;**15**:451–479. doi:[10.1146/annurev-clinpsy-050718-095754](https://doi.org/10.1146/annurev-clinpsy-050718-095754).
15. Manoach DS, et al. Reduced overnight consolidation of procedural learning in chronic medicated schizophrenia is related to specific sleep stages. *J Psychiatr Res.* 2010;**44**(2):112–120. doi:[10.1016/j.jpsychires.2009.06.011](https://doi.org/10.1016/j.jpsychires.2009.06.011).
16. Kozhemiako N, et al. Non-rapid eye movement sleep and wake neurophysiology in schizophrenia. *eLife.* 2022;**11**:e76211. doi:[10.7554/eLife.76211](https://doi.org/10.7554/eLife.76211).
17. Rauchs G, et al. Is there a link between sleep changes and memory in Alzheimer's disease? *Neuroreport.* 2008;**19**(11):1159–1162. doi:[10.1097/WNR.0b013e32830867c4](https://doi.org/10.1097/WNR.0b013e32830867c4).
18. Weng Y-Y, et al. Sleep spindle abnormalities related to Alzheimer's disease: a systematic mini-review. *Sleep Med.* 2020;**75**:37–44. doi:[10.1016/j.sleep.2020.07.044](https://doi.org/10.1016/j.sleep.2020.07.044).
19. Winer JR, et al. Sleep as a potential biomarker of tau and β -amyloid burden in the human brain. *J Neurosci.* 2019;**39**(32):6315–6324. doi:[10.1523/JNEUROSCI.0503-19.2019](https://doi.org/10.1523/JNEUROSCI.0503-19.2019).
20. Tessier S, et al. Intelligence measures and stage 2 sleep in typically-developing and autistic children. *Int J Psychophysiol.* 2015;**97**(1):58–65. doi:[10.1016/j.ijpsycho.2015.05.003](https://doi.org/10.1016/j.ijpsycho.2015.05.003).
21. Limoges E, et al. Atypical sleep architecture and the autism phenotype. *Brain.* 2005;**128**(Pt 5):1049–1061. doi:[10.1093/brain/awh425](https://doi.org/10.1093/brain/awh425).
22. Purcell SM, et al. Characterizing sleep spindles in 11,630 individuals from the National Sleep Research Resource. *Nat Commun.* 2017;**8**:15930. doi:[10.1038/ncomms15930](https://doi.org/10.1038/ncomms15930).
23. Djonlagic I, et al. Macro and micro sleep architecture and cognitive performance in older adults. *Nat Hum Behav.* 2021;**5**(1):123–145. doi:[10.1038/s41562-020-00964-y](https://doi.org/10.1038/s41562-020-00964-y).
24. Mander BA, et al. Sleep and human aging. *Neuron.* 2017;**94**(1):19–36. doi:[10.1016/j.neuron.2017.02.004](https://doi.org/10.1016/j.neuron.2017.02.004).
25. Martin N, et al. Topography of age-related changes in sleep spindles. *Neurobiol Aging.* 2013;**34**(2):468–476. doi:[10.1016/j.neurobiolaging.2012.05.020](https://doi.org/10.1016/j.neurobiolaging.2012.05.020).
26. Mander BA, et al. Impaired prefrontal sleep spindle regulation of hippocampal-dependent learning in older adults. *Cereb Cortex.* 2014;**24**(12):3301–3309. doi:[10.1093/cercor/bht188](https://doi.org/10.1093/cercor/bht188).
27. Bódizs R, et al. The individual adjustment method of sleep spindle analysis: methodological improvements and roots in the fingerprint paradigm. *J Neurosci Methods.* 2009;**178**(1):205–213. doi:[10.1016/j.jneumeth.2008.11.006](https://doi.org/10.1016/j.jneumeth.2008.11.006).
28. Finelli LA, et al. Individual “fingerprints” in human sleep EEG topography. *Neuropsychopharmacology.* 2001;**25**(suppl 5):S57–S62. doi:[10.1016/S0893-133X\(01\)00320-7](https://doi.org/10.1016/S0893-133X(01)00320-7).
29. De Gennaro L, et al. An electroencephalographic fingerprint of human sleep. *Neuroimage.* 2005;**26**(1):114–122. doi:[10.1016/j.neuroimage.2005.01.020](https://doi.org/10.1016/j.neuroimage.2005.01.020).
30. Loomis AL, et al. Cerebral states during sleep, as studied by human brain potentials. *J Exp Psychol.* 1937;**21**(2):127–144. doi:[10.1037/h0057431](https://doi.org/10.1037/h0057431).
31. Loomis AL, et al. Potential rhythms of the cerebral cortex during sleep. *Science.* 1935;**81**(2111):597–598. doi:[10.1126/science.81.2111.597](https://doi.org/10.1126/science.81.2111.597).
32. Silber MH, et al. The visual scoring of sleep in adults. *J Clin Sleep Med.* 2007;**3**(2):121–131. doi:[10.5664/jcsm.26814](https://doi.org/10.5664/jcsm.26814).
33. Warby SC, et al. Sleep-spindle detection: crowdsourcing and evaluating performance of experts, non-experts and automated methods. *Nat Methods.* 2014;**11**(4):385–392. doi:[10.1038/nmeth.2855](https://doi.org/10.1038/nmeth.2855).
34. Dimitrov T, He M, Stickgold R, Prerau MJ. Sleep spindles comprise a subset of a broader class of electroencephalogram events. *Sleep.* 2021;**44**(9). doi:[10.1093/sleep/zsab099](https://doi.org/10.1093/sleep/zsab099).
35. Brown RE, et al. Control of sleep and wakefulness. *Physiol Rev.* 2012;**92**(3):1087–1187. doi:[10.1152/physrev.00032.2011](https://doi.org/10.1152/physrev.00032.2011).
36. Steriade M, Jones EG, Llinas RR. *Thalamic Oscillations and Signaling (Neuroscience Institute Monograph Series).* 1st ed. New York, USA: Wiley-Interscience; 1990:431.
37. Steriade M. Thalamic origin of sleep spindles: Morison and Bassett (1945). *J Neurophysiol.* 1995;**73**(3):921–922. doi:[10.1152/jn.1995.73.3.921](https://doi.org/10.1152/jn.1995.73.3.921).
38. Jacobsen RB, et al. GABA(B) and NMDA receptors contribute to spindle-like oscillations in rat thalamus in vitro. *J Neurophysiol.* 2001;**86**(3):1365–1375. doi:[10.1152/jn.2001.86.3.1365](https://doi.org/10.1152/jn.2001.86.3.1365).
39. Percival DB. *Spectral Analysis for Physical Applications: Multitaper and Conventional Univariate Techniques.* Cambridge, UK: Cambridge University Press; 2010:612.
40. Prerau MJ, et al. Sleep neurophysiological dynamics through the lens of multitaper spectral analysis. *Physiology (Bethesda).* 2017;**32**(1):60–92. doi:[10.1152/physiol.00062.2015](https://doi.org/10.1152/physiol.00062.2015).

41. Olbrich E, et al. The multiple time scales of sleep dynamics as a challenge for modelling the sleeping brain. *Philos Transact A Math Phys Eng Sci.* 2011;**369**(1952):3884–3901. doi:[10.1098/rsta.2011.0082](https://doi.org/10.1098/rsta.2011.0082).
42. Olbrich E, et al. Analysis of the temporal organization of sleep spindles in the human sleep EEG using a phenomenological modeling approach. *J Biol Phys.* 2008;**34**(3–4):241–249. doi:[10.1007/s10867-008-9078-z](https://doi.org/10.1007/s10867-008-9078-z).
43. Olbrich E, et al. Analysis of oscillatory patterns in the human sleep EEG using a novel detection algorithm. *J Sleep Res.* 2005;**14**(4):337–346. doi:[10.1111/j.1365-2869.2005.00475.x](https://doi.org/10.1111/j.1365-2869.2005.00475.x).
44. Romero-Zaliz R, Reinoso-Gordo JF. An updated review on watershed algorithms. In: Cruz Corona C, ed. *Soft Computing for Sustainability Science. Studies in Fuzziness and Soft Computing.* Vol 358. Cham, Switzerland: Springer International Publishing; 2018:235–258. doi:[10.1007/978-3-319-62359-7_12](https://doi.org/10.1007/978-3-319-62359-7_12).
45. Kornilov A, et al. An overview of watershed algorithm implementations in open source libraries. *J Imaging* 2018;**4**(10):123123. doi:[10.3390/jimaging4100123](https://doi.org/10.3390/jimaging4100123).
46. Čomić L, De Floriani L, Magillo P, Iuricich F. Watershed algorithms. In: *Morphological Modeling of Terrains and Volume Data. Springerbriefs in Computer Science.* New York: Springer. 2014:59–68. doi:[10.1007/978-1-4939-2149-2_4](https://doi.org/10.1007/978-1-4939-2149-2_4).
47. Dauwels J, et al. A comparative study of synchrony measures for the early diagnosis of Alzheimer's disease based on EEG. *Neuroimage.* 2010;**49**(1):668–693. doi:[10.1016/j.neuroimage.2009.06.056](https://doi.org/10.1016/j.neuroimage.2009.06.056).
48. Barroso-García V, et al. Bispectral analysis of overnight airflow to improve the pediatric sleep apnea diagnosis. *Comput Biol Med.* 2021;**129**:104167. doi:[10.1016/j.compbiomed.2020.104167](https://doi.org/10.1016/j.compbiomed.2020.104167).
49. Kearse LA, et al. Bispectral analysis of the electroencephalogram correlates with patient movement to skin incision during propofol/nitrous oxide anesthesia. *Anesthesiology.* 1994;**81**(6):1365–1370. doi:[10.1097/0000542-199412000-00010](https://doi.org/10.1097/0000542-199412000-00010).
50. Sigl JC, et al. An introduction to bispectral analysis for the electroencephalogram. *J Clin Monit* 1994;**10**(6):392–404. doi:[10.1007/BF01618421](https://doi.org/10.1007/BF01618421).
51. Pedrão RAA, et al. Viability and validity of the bispectral index to measure sleep in patients in the intensive care unit. *Rev Bras Ter Intensiva* 2020;**32**(4):535–541. doi:[10.5935/0103-507X.20200083](https://doi.org/10.5935/0103-507X.20200083).
52. Nieuwenhuijs D, Coleman EL, Douglas NJ, Drummond GB, Dahan A. Bispectral index values and spectral edge frequency at different stages of physiologic sleep. *Anesth Analg.* 2002;**94**(1):125–129. doi:[10.1097/0000539-200201000-00024](https://doi.org/10.1097/0000539-200201000-00024).
53. Prerau MJ, et al. Tracking the sleep onset process: an empirical model of behavioral and physiological dynamics. *PLoS Comput Biol.* 2014;**10**(10):e1003866. doi:[10.1371/journal.pcbi.1003866](https://doi.org/10.1371/journal.pcbi.1003866).
54. Younes M, et al. Odds ratio product of sleep EEG as a continuous measure of sleep state. *Sleep.* 2015;**38**(4):641–654. doi:[10.5665/sleep.4588](https://doi.org/10.5665/sleep.4588).
55. Burioka N, et al. Approximate entropy in the electroencephalogram during wake and sleep. *Clin EEG Neurosci.* 2005;**36**(1):21–24. doi:[10.1177/155005940503600106](https://doi.org/10.1177/155005940503600106).
56. Fell J, et al. Discrimination of sleep stages: a comparison between spectral and nonlinear EEG measures. *Electroencephalogr Clin Neurophysiol.* 1996;**98**(5):401–410. doi:[10.1016/0013-4694\(96\)95636-9](https://doi.org/10.1016/0013-4694(96)95636-9).
57. McKinney SM, et al. Covert waking brain activity reveals instantaneous sleep depth. *PLoS One.* 2011;**6**(3):e17351. doi:[10.1371/journal.pone.0017351](https://doi.org/10.1371/journal.pone.0017351).
58. Lendner JD, et al. An electrophysiological marker of arousal level in humans. *eLife* 2020;**9**:e55092. doi:[10.7554/eLife.55092](https://doi.org/10.7554/eLife.55092).
59. Gao R, et al. Inferring synaptic excitation/inhibition balance from field potentials. *Neuroimage.* 2017;**158**:70–78. doi:[10.1016/j.neuroimage.2017.06.078](https://doi.org/10.1016/j.neuroimage.2017.06.078).
60. Borbély AA. A two process model of sleep regulation. *Hum Neurobiol.* 1982;**1**(3):195–204.
61. Aeschbach D, et al. All-night dynamics of the human sleep EEG. *J Sleep Res.* 1993;**2**(2):70–81.
62. Borbély AA. Refining sleep homeostasis in the two-process model. *J Sleep Res.* 2009;**18**(1):1–2. doi:[10.1111/j.1365-2869.2009.00750.x](https://doi.org/10.1111/j.1365-2869.2009.00750.x).
63. Borbély AA, et al. Sleep homeostasis and models of sleep regulation. *J Biol Rhythms.* 1999;**14**(6):557–568. doi:[10.1177/074873099129000894](https://doi.org/10.1177/074873099129000894).
64. Mikutta C, et al. Phase-amplitude coupling of sleep slow oscillatory and spindle activity correlates with overnight memory consolidation. *J Sleep Res.* 2019;**28**(6):e12835. doi:[10.1111/jsr.12835](https://doi.org/10.1111/jsr.12835).
65. Muehlroth BE, et al. Precise slow oscillation-spindle coupling promotes memory consolidation in younger and older adults. *Sci Rep.* 2019;**9**(1):1940. doi:[10.1038/s41598-018-36557-z](https://doi.org/10.1038/s41598-018-36557-z).
66. Hahn MA, et al. Slow oscillation-spindle coupling predicts enhanced memory formation from childhood to adolescence. *eLife.* 2020;**9**:e53730. doi:[10.7554/eLife.53730](https://doi.org/10.7554/eLife.53730).
67. Bergmann TO, et al. Phase-Amplitude coupling: a general mechanism for memory processing and synaptic plasticity? *Neuron.* 2018;**97**(1):10–13. doi:[10.1016/j.neuron.2017.12.023](https://doi.org/10.1016/j.neuron.2017.12.023).
68. Kovesi P. Good colour maps: how to design them. ArXiv, abs/1509.03700. 2015. doi:[10.48550/arxiv.1509.03700](https://doi.org/10.48550/arxiv.1509.03700).
69. Benjamini Y, et al. The control of the false discovery rate in multiple testing under dependency. *Ann Statist.* 2001;**29**(4):1165–1188. doi:[10.1214/aos/1013699998](https://doi.org/10.1214/aos/1013699998).
70. Massey FJ. The Kolmogorov-Smirnov test for goodness of fit. *J Am Stat Assoc.* 1951;**46**(253):68–78. doi:[10.1080/01621459.1951.10500769](https://doi.org/10.1080/01621459.1951.10500769).
71. Bronez TP. On the performance advantage of multitaper spectral analysis. *IEEE Trans Signal Process.* 1992;**40**(12):2941–2946. doi:[10.1109/78.175738](https://doi.org/10.1109/78.175738).
72. Thomson DJ. Spectrum estimation and harmonic analysis. *Proc IEEE.* 1982;**70**(9):1055–1096. doi:[10.1109/proc.1982.12433](https://doi.org/10.1109/proc.1982.12433).
73. Cox R, et al. Individual differences in frequency and topography of slow and fast sleep spindles. *Front Hum Neurosci.* 2017;**11**:433. doi:[10.3389/fnhum.2017.00433](https://doi.org/10.3389/fnhum.2017.00433).
74. Purcell S. Sleep spindles and schizophrenia genetics. *Neuropsychopharmacology.* 2017;**42**:S36–S37.
75. Prerau MJ, et al. Tracking non-stationary spectral peak structure in EEG data. *Annu Int Conf IEEE Eng Med Biol Soc* 2013;**2013**:417–420. doi:[10.1109/EMBC.2013.6609525](https://doi.org/10.1109/EMBC.2013.6609525).
76. Stokes PA, et al. Estimation of time-varying spectral peaks and decomposition of EEG spectrograms. *IEEE Access.* 2020;**8**:218257–218278. doi:[10.1109/access.2020.3042737](https://doi.org/10.1109/access.2020.3042737).
77. De Carli F, et al. Quantitative analysis of sleep EEG microstructure in the time-frequency domain. *Brain Res Bull.* 2004;**63**(5):399–405. doi:[10.1016/j.brainresbull.2003.12.013](https://doi.org/10.1016/j.brainresbull.2003.12.013).
78. Achermann P, et al. A model of human sleep homeostasis based on EEG slow-wave activity: quantitative comparison of data and simulations. *Brain Res Bull.* 1993;**31**(1–2):97–113. doi:[10.1016/0361-9230\(93\)90016-5](https://doi.org/10.1016/0361-9230(93)90016-5).
79. Gonzalez CE, et al. Theta bursts precede, and spindles follow, cortical and thalamic downstates in human NREM sleep. *J Neurosci.* 2018;**38**(46):9989–10001. doi:[10.1523/JNEUROSCI.0476-18.2018](https://doi.org/10.1523/JNEUROSCI.0476-18.2018).
80. Ferrarelli F, et al. Reduced sleep spindle activity in schizophrenia patients. *Am J Psychiatry.* 2007;**164**(3):483–492. doi:[10.1176/ajp.2007.164.3.483](https://doi.org/10.1176/ajp.2007.164.3.483).
81. Ferrarelli F, et al. Thalamic dysfunction in schizophrenia suggested by whole-night deficits in slow and fast spindles.

- Am J Psychiatry*. 2010;**167**(11):1339–1348. doi:[10.1176/appi.ajp.2010.09121731](https://doi.org/10.1176/appi.ajp.2010.09121731).
82. Manoach DS, et al. Targeting sleep oscillations to improve memory in schizophrenia. *Schizophr Res*. 2020;**221**:63–70. doi:[10.1016/j.schres.2020.01.010](https://doi.org/10.1016/j.schres.2020.01.010).
 83. Purcell S, et al. Characterizing sleep spindles in 11,630 individuals from the national sleep research resource. *Neuropsychopharmacology*. **41**:S599–S600. doi:[10.1038/ncomms15930](https://doi.org/10.1038/ncomms15930).
 84. Werth E, et al. Spindle frequency activity in the sleep EEG: individual differences and topographic distribution. *Electroencephalogr Clin Neurophysiol*. 1997;**103**(5):535–542. doi:[10.1016/s0013-4694\(97\)00070-9](https://doi.org/10.1016/s0013-4694(97)00070-9).
 85. Mölle M, et al. Grouping of spindle activity during slow oscillations in human non-rapid eye movement sleep. *J Neurosci*. 2002;**22**(24):10941–10947. doi:[10.1523/jneurosci.22-24-10941.2002](https://doi.org/10.1523/jneurosci.22-24-10941.2002).
 86. French AP. *Vibrations and Waves*. 1st ed. London, UK: Taylor & Francis; 1971:325.
 87. McConnell BV, et al. The aging slow wave: a shifting amalgam of distinct slow wave and spindle coupling subtypes define slow wave sleep across the human lifespan. *Sleep*. 2021;**44**(10). doi:[10.1093/sleep/zsab125](https://doi.org/10.1093/sleep/zsab125).
 88. Cantero JL, et al. Human alpha oscillations in wakefulness, drowsiness period, and REM sleep: different electroencephalographic phenomena within the alpha band. *Neurophysiol Clin*. 2002;**32**(1):54–71. doi:[10.1016/s0987-7053\(01\)00289-1](https://doi.org/10.1016/s0987-7053(01)00289-1).
 89. Cantero JL, et al. Spectral structure and brain mapping of human alpha activities in different arousal states. *Neuropsychobiology*. 1999;**39**(2):110–116. doi:[10.1159/000026569](https://doi.org/10.1159/000026569).
 90. Hughes SW, et al. Thalamic mechanisms of EEG alpha rhythms and their pathological implications. *Neuroscientist*. 2005;**11**(4):357–372. doi:[10.1177/1073858405277450](https://doi.org/10.1177/1073858405277450).
 91. Martinez D, et al. Light sleep and sleep time misperception - relationship to alpha-delta sleep. *Clin Neurophysiol*. 2010;**121**(5):704–711. doi:[10.1016/j.clinph.2010.01.005](https://doi.org/10.1016/j.clinph.2010.01.005).
 92. Dauvilliers Y, et al. Sleep in fibromyalgia: review of clinical and polysomnographic data. *Neurophysiol Clin*. 2001;**31**(1):18–33. doi:[10.1016/s0987-7053\(00\)00240-9](https://doi.org/10.1016/s0987-7053(00)00240-9).
 93. Zhao W, et al. EEG spectral analysis in insomnia disorder: a systematic review and meta-analysis. *Sleep Med Rev*. 2021;**59**:101457. doi:[10.1016/j.smrv.2021.101457](https://doi.org/10.1016/j.smrv.2021.101457).
 94. Stone KC, et al. Nonrestorative sleep. *Sleep Med Rev*. 2008;**12**(4):275–288. doi:[10.1016/j.smrv.2007.12.002](https://doi.org/10.1016/j.smrv.2007.12.002).
 95. Cantero JL, et al. Alpha burst activity during human REM sleep: descriptive study and functional hypotheses. *Clin Neurophysiol*. 2000;**111**(5):909–915. doi:[10.1016/s1388-2457\(99\)00318-1](https://doi.org/10.1016/s1388-2457(99)00318-1).
 96. Brodbeck V, et al. EEG microstates of wakefulness and NREM sleep. *Neuroimage*. 2012;**62**(3):2129–2139. doi:[10.1016/j.neuroimage.2012.05.060](https://doi.org/10.1016/j.neuroimage.2012.05.060).
 97. Katayama H, et al. Classes of multichannel EEG microstates in light and deep hypnotic conditions. *Brain Topogr*. 2007;**20**(1):7–14. doi:[10.1007/s10548-007-0024-3](https://doi.org/10.1007/s10548-007-0024-3).
 98. Khanna A, et al. Microstates in resting-state EEG: current status and future directions. *Neurosci Biobehav Rev*. 2015;**49**:105–113. doi:[10.1016/j.neubiorev.2014.12.010](https://doi.org/10.1016/j.neubiorev.2014.12.010).
 99. Kokkinos V, et al. The hippocampal barque: an epileptiform but non-epileptic hippocampal entity. *Front Hum Neurosci*. 2020;**14**:92. doi:[10.3389/fnhum.2020.00092](https://doi.org/10.3389/fnhum.2020.00092).
 100. Jiang X, et al. Coordination of human hippocampal sharpwave ripples during nrem sleep with cortical theta bursts, spindles, downstates, and upstates. *J Neurosci*. 2019;**39**(44):8744–8761. doi:[10.1523/JNEUROSCI.2857-18.2019](https://doi.org/10.1523/JNEUROSCI.2857-18.2019).
 101. Adra N, et al. Optimal spindle detection parameters for predicting cognitive performance. *Sleep*. 2022;**45**(4). doi:[10.1093/sleep/zsac001](https://doi.org/10.1093/sleep/zsac001).
 102. Voytek B, et al. Age-related changes in 1/f neural electrophysiological noise. *J Neurosci*. 2015;**35**(38):13257–13265. doi:[10.1523/JNEUROSCI.2332-14.2015](https://doi.org/10.1523/JNEUROSCI.2332-14.2015).
 103. MATLAB. (2022a). Natick, Massachusetts: The MathWorks Inc.